PAPER

Check for updates

Magnetic carbon nanotube-catalyzed multicomponent synthesis of 5-substituted-1H-tetrazoles†

Ahmad Sajjadi, [ID] *[a] Vicky Jain,[b] Suhas Ballal,[c] Munthar Kadhim Abosaoda,[de] Abhayveer Singh,[f] T. Krithiga,[g] Subhashree Ray[h] and Naveen Chandra Talniya[ij]

This study presents a pioneering approach with the introduction of a novel magnetic carbon nanotube composite, $AlFe_2O_4$–MWCNT–TEA–Ni(II), designed as an efficient catalyst for the multicomponent synthesis of 5-substituted-1H-tetrazoles (18 examples, yields 89–98%). The primary objectives were to develop and evaluate this catalyst's ability to promote the formation of tetrazoles under eco-friendly conditions. The methods involved synthesizing the catalyst by combining $AlFe_2O_4$, MWCNTs, TEA, and Ni(II), then testing its catalytic activity using various aromatic aldehydes, hydroxylamine, and sodium azide in DMF at 50 °C. The reaction parameters, including temperature, catalyst amount, and reaction time, were optimized for maximum yield and selectivity. Results showed that the catalyst achieved high yields of tetrazoles and demonstrated significant selectivity in a remarkably short reaction time, showcasing its exceptional efficiency. The magnetism of $AlFe_2O_4$ facilitated easy recovery and recyclability (seven runs), underscoring the catalyst's sustainability. This system's advantages include its high activity, reusability, and environmentally friendly nature, making it a promising approach for green nitrogen-rich heterocycle synthesis. Prospects involve exploring the catalyst's potential in large-scale applications, expanding its use to other heterocyclic syntheses, and investigating its performance with different substrates. This work underscores the significant role of integrating magnetic nanomaterials into catalytic systems to promote sustainable and efficient organic synthesis methods, offering a promising future for the field.

[a]Young Researchers and Elite Club, Tehran Branch, Islamic Azad University, Tehran, Iran. E-mail: sajjadiahmmad@gmail.com

[b]Marwadi University Research Center, Department of Chemistry, Faculty of Science Marwadi University, Rajkot-360003, Gujarat, India. E-mail: vicky.jain@marwadieducation.edu.in

[c]Department of Chemistry and Biochemistry, School of Sciences, JAIN (Deemed to be University), Bangalore, Karnataka, India. E-mail: b.suhas@jainuniversity.ac.in

[d]College of pharmacy, the Islamic University, Najaf, Iraq. E-mail: muntherabosoda@iunajaf.edu.iq

[e]College of pharmacy, The Islamic University of Al Diwaniyah, Al Diwaniyah, Iraq

[f]Centre for Research Impact & Outcome, Chitkara University Institute of Engineering and Technology, Chitkara University, Rajpura, 140401, Punjab, India. E-mail: abhayveer_singh@outlook.com

[g]Department of Chemistry, Sathyabama Institute of Science and Technology, Chennai, Tamil Nadu, India. E-mail: krithiga.chemistry@sathyabama.ac.in

[h]Department of Biochemistry IMS and SUM Hospital, Siksha 'O' Anusandhan (Deemed to be University), Bhubaneswar, Odisha-751003, India. E-mail: sbhashreeray@soa.ac.in

[i]Department of Chemistry, Graphic Era Hill University, Dehradun, India. E-mail: ntalniya@gehu.ac.in

[j]Centre for Promotion of Research, Graphic Era Deemed to be University, Dehradun, Uttarakhand-248002, India

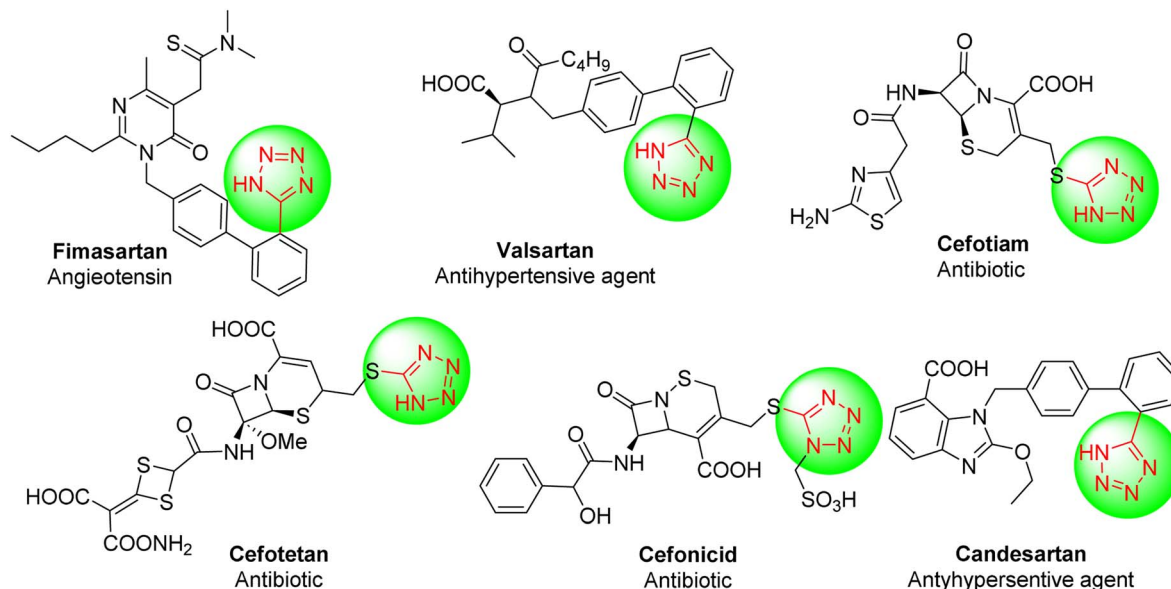† Electronic supplementary information (ESI) available. See DOI: https://doi.org/10.1039/d5ra02641e

Introduction

Tetrazoles are five-membered heterocyclic compounds with four nitrogen atoms and one carbon.[1–3] 5-Substituted-1H-tetrazoles are important due to their unique properties and diverse uses in medicine and industry. They serve as key pharmacophores in drug development, mimicking carboxylic acids with improved stability and resistance to degradation.[4–6]

Furthermore, introducing substituents at the 5-position allows for fine-tuning of the compound's physicochemical properties, such as lipophilicity and solubility, which are critical for drug delivery and efficacy.[7,8] The tetrazoles are now known for their roles in pharmaceuticals, including as antagonists,[9,10] HIV,[11] inhibitors,[12,13] antiviral drugs,[14] antibiotics,[15] anticancer,[16] antimicrobials,[17] and antioxidants.[18] Moreover, the unique electronic and physical properties of tetrazoles make them valuable in the development of energy storage materials and chemosensors, adding to their significance in modern scientific research.[19–21] 5-Substituted-1H-tetrazoles are widely used beyond medicine in industries like explosives, propellants, pyrotechnics, metalworking fluids, and coatings (Fig. 1). They also serve as ligands in coordination chemistry to form stable metal complexes.[22–26]

Fig. 1 Some bioactive compounds contain structures containing substituted 5-phenyl-1*H*-tetrazole derivatives.

Multicomponent reactions (MCRs) are efficient methods in organic synthesis that assemble complex molecules from three or more reactants in one step. They streamline synthesis, reduce waste, and increase molecular diversity. Their value is particularly pronounced in the production of pharmaceuticals, agrochemicals, and materials, where their unique capabilities are harnessed. MCRs involve multiple reactants reacting simultaneously in a single vessel, forming products that incorporate most starting atoms through *in situ* intermediates, leading to fewer steps and purifications.[27–33]

Magnetic carbon nanotubes (MCNTs) are hybrid materials that blend the unique properties of carbon nanotubes (CNTs) with magnetic nanoparticles. They possess a high surface area, stability, electrical conductivity, and magnetic responsiveness. MCNTs are utilized as reusable and magnetically separable catalysts in catalysis and sustainable chemistry.[34–40] MCNTs are typically created by decorating CNTs with magnetic nanoparticles like Fe_3O_4, $CoFe_2O_4$, or Ni, using *in situ* (during CNT growth *via* methods like CVD or sol–gel) or *ex situ* (attaching pre-made MNPs after CNT synthesis) approaches. A significant advancement in their performance is achieved by functionalizing MCNTs with oxygen groups, which improves nanoparticle attachment and catalytic activity. They are widely used as catalysts or supports in oxidation, reduction, hydrogenation, and coupling reactions.[41–49]

Tetrazoles are synthesized using traditional methods, including the combination of azides and nitriles, amines and orthoesters, or isocyanides. The choice of method depends on the desired substituents, functional groups, and the need for scalability. Recent advancements in catalysts and reaction conditions have enhanced the capability to produce complex, functionalized tetrazole derivatives.[50–60] The AlFe₂O₄–MWCNT–TEA–Ni(ɪɪ) catalyst unites components that work together: AlFe₂O₄ provides magnetic support and stability, MWCNTs enhance surface area and conductivity, TEA stabilizes Ni(ɪɪ)

ions, and Ni(ɪɪ) promotes tetrazole synthesis. Together, these improve catalytic activity and durability.[61–66]

This study focuses on developing and characterizing the AlFe₂O₄–MWCNT–TEA–Ni(ɪɪ) catalyst for efficient, sustainable synthesis of 5-substituted-1*H*-tetrazoles *via* cycloaddition. It aims to optimize reaction conditions, understand the reaction mechanism, and evaluate the catalyst's potential for green, scalable applications. This catalyst, with its unique combination of magnetic support, high surface area, stabilization, and catalysis, offers a cost-effective, eco-friendly alternative. Its adoption could significantly advance organic synthesis, particularly in medicinal chemistry and materials science, and contribute to innovative solutions in healthcare and industry.

Results and discussion

A novel, practical, eco-friendly, and cost-effective heterogeneous catalyst, AlFe₂O₄–MWCNT–TEA–Ni(ɪɪ), was developed for the growth of stable metallic nickel(ɪɪ) nanoparticles was employed in the synthesis of 5-substituted 1*H*-tetrazole derivatives *via* an MCR approach. The primary objective of this study is to develop and characterize a novel nanocatalyst system (AlFe₂O₄–MWCNT–TEA–Ni(ɪɪ)) for the efficient and sustainable synthesis of tetrazole derivatives, explicitly targeting the click reaction between aromatic aldehydes, hydroxylamine, and sodium azide at 50 °C in dimethylformamide. The focus is specifically on the multicomponent reaction between benzonitrile and sodium azide to synthesize 5-phenyl-1*H*-tetrazole, as depicted in Scheme 1. This research addresses the inefficiencies previously
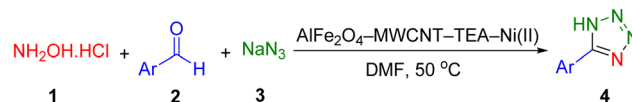
Scheme 1 Synthesis of 5-phenyl-1*H*-tetrazoles.
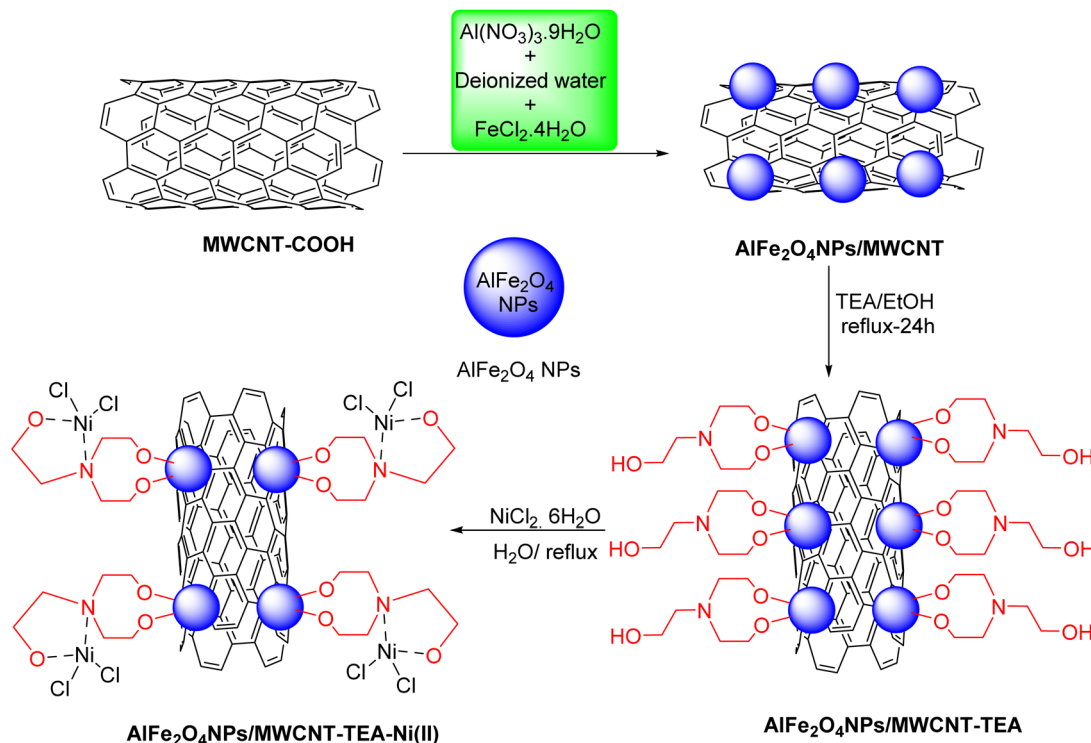
Scheme 2 Procedure for the preparation of AlFe$_2$O$_4$–MWCNT–TEA–Ni(II).

encountered with conventional methods by enhancing the reaction conditions and improving the catalytic performance. Moreover, this study intends to explore the reusability and stability of the developed bio-nanocatalyst, thereby establishing its potential application in continuous flow processes.

The synthesis of the AlFe$_2$O$_4$–MWCNT–TEA–Ni(II) nanocatalyst, as depicted in Scheme 2, involves a multi-step process:

Al(NO$_3$)$_3$·9H$_2$O and FeCl$_2$·4H$_2$O are mixed in deionized water. The resulting solution is combined with MWCNT–COOH (carboxyl-functionalized multi-walled carbon nanotubes). This mixture undergoes a reaction (specific conditions not provided in the image) to form the AlFe$_2$O$_4$ NPs/MWCNT composite.

Functionalization with TEA

The AlFe$_2$O$_4$ NPs/MWCNT composite is reacted with triethanolamine (TEA) in ethanol (EtOH) under reflux for 24 hours. This step introduces TEA functional groups onto the composite, resulting in AlFe$_2$O$_4$ NPs/MWCNT–TEA.

Nickel incorporation

The AlFe$_2$O$_4$ NPs/MWCNT-TEA are further reacted with NiCl$_2$·6H$_2$O in water under reflux. This process incorporates nickel ions into the structure, forming the final AlFe$_2$O$_4$–MWCNT–TEA–Ni(II) nanocatalyst.

Characterization of the nanocatalyst

Fig. 2 illustrates the Fourier Transform Infrared (FT-IR) spectra of three distinct nanomaterials: AlFe$_2$O$_4$@MWCNT, AlFe$_2$O$_4$@-MWCNT–TEA, and AlFe$_2$O$_4$@MWCNT–TEA–Ni(II) NPs. The analysis of these spectra provides insights into the functional groups present in each material and the interactions that may influence their catalytic properties.

The spectrum of AlFe$_2$O$_4$@MWCNT, represented by the red line, displays characteristic peaks corresponding to metal–oxygen vibrations, particularly in the 400 to 600 cm^{-1}, indicating the presence of spinel-type ferrites. Additionally, broad absorption bands around 3400 cm^{-1} suggest the presence of
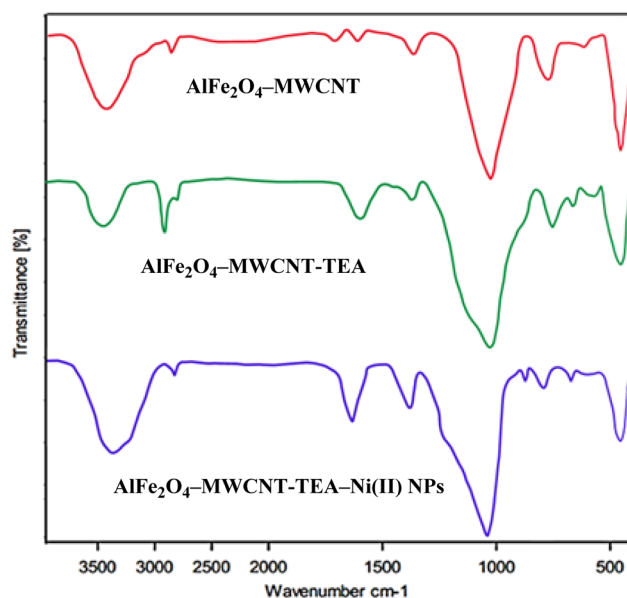
Fig. 2 FT-IR spectrums of AlFe$_2$O$_4$@MWCNT, AlFe$_2$O$_4$@MWCNT–TEA, and AlFe$_2$O$_4$@MWCNT–TEA–Ni(II) nanocatalyst.

hydroxyl groups (−OH), likely due to moisture or surface hydroxylation.

Contrastingly, the spectrum for AlFe$_2$O$_4$@MWCNT–TEA, shown in green, unveils additional peaks corresponding to the functional groups associated with triethanolamine (TEA). Notably, there are distinct peaks around 1500 cm^{-1} and 1700 cm^{-1}, which can be attributed to C–N stretching vibrations and carbonyl (C=O) stretching vibrations, respectively. This confirms the successful incorporation of TEA into the composite structure and hints at the potential of TEA to significantly enhance catalytic activity through its interactions with the metal oxide framework.

The blue line depicts the spectrum for AlFe$_2$O$_4$@MWCNT–TEA–Ni(II) NPs. Here, new peaks emerge, confirming the successful incorporation of nickel ions within the nanocatalyst. The characteristic Ni–O stretching vibrations appear around 600 cm^{-1}, providing strong evidence of the successful doping of nickel into the composite material. The shifts in peak positions compared to previous spectra suggest changes in bond character and coordination environments due to nickel incorporation, further validating our research.

Comparative analysis of these FT-IR spectra highlights how each modification affects the chemical environment within the nanocomposites. The introduction of TEA not only contributes additional functional groups but also enhances the interaction potential between reactants and active sites on the catalyst surface. Furthermore, incorporating nickel modifies structural integrity and catalytic properties by introducing new active sites while maintaining favorable interactions with other components.

These findings underscore the importance of chemical modifications in tailoring nanocatalysts for specific applications. The distinct spectral features observed across these materials indicate that strategic design through functionalization can significantly impact their performance in catalytic processes.

Fig. 3 presents the Energy Dispersive X-ray (EDX) analysis of the AlFe$_2$O$_4$@MWCNT–TEA–Ni(II) catalyst, providing essential insights into its elemental composition. The EDX spectrum displays several prominent peaks corresponding to the characteristic X-ray emissions of various elements in the nanocatalyst. Notably, peaks for oxygen (O Kα), iron (Fe Lα and Fe Kα), aluminum (Al Kα), nickel (Ni Lα and Ni Kα), nitrogen (N Kα), and carbon (C Kα) are identifiable, indicating a successful incorporation of these elements into the composite structure.

The peak intensity indicates the relative abundance of each element within the sample. The most significant peak corresponds to iron, suggesting that it is a major component of the catalyst, consistent with its role as a primary constituent of the spinel ferrite structure. The presence of aluminum further corroborates the formation of AlFe$_2$O$_4$. At the same time, the detection of nickel signifies its successful doping into the nanocomposite, which may enhance catalytic activity due to nickel's known properties as an active catalyst in various reactions.

Moreover, the presence of nitrogen and carbon signals that triethanolamine (TEA) is indeed integrated within the structure, potentially influencing both the catalyst's physical properties and reactivity. The carbon peak may also arise from residual carbon from multi-walled carbon nanotubes (MWCNTs), which serve as a support matrix enhancing surface area and stability.

When comparing this EDX data with other reported catalysts in the literature, it becomes evident that this specific formulation exhibits a favorable balance between metal oxides and organic components. Many traditional catalysts often lack such a diverse elemental composition, which can limit their efficiency due to insufficient active sites or poor structural integrity. The incorporation of TEA not only aids in stabilizing metal ions but also facilitates interactions that can improve overall catalytic performance.

EDX analysis provides crucial information regarding the elemental makeup of AlFe$_2$O$_4$@MWCNT–TEA–Ni(II), affirming its potential as an effective catalyst. The distinct peaks observed reflect a well-designed composite that leverages both inorganic and organic components to optimize catalytic activity. Future research should focus on correlating these compositional attributes with specific catalytic performance metrics to elucidate further how modifications impact reaction mechanisms and efficiencies in practical applications.

Fig. 4 showcases the Brunauer–Emmett–Teller (BET) analysis of the AlFe$_2$O$_4$@MWCNT–TEA–Ni(II) nanocatalyst, unveiling the intriguing relationship between the adsorbed volume and relative pressure (p/p_0). The graph unveils two distinct curves, each a window into the nanocatalyst's unique adsorption behavior at varying pressures. As the relative pressure escalates, a gradual surge in the volume of gas adsorbed becomes apparent, particularly as it nears a pressure of approximately 0.8 p/p_0. This trend hints at the nanocatalyst's significant porosity, a feature that could hold the key to its potential in gas adsorption applications.

The quantitative measurements from this analysis unveil a striking fact: the specific surface area of the AlFe$_2$O$_4$@MWCNT–TEA–Ni(II) nanocatalyst is a remarkable 250 m^2 g^{-1}. This high surface area, a testament to the nanocatalyst's potential, is a boon for catalytic applications, providing many active sites for reactions. Furthermore, the pore diameter is
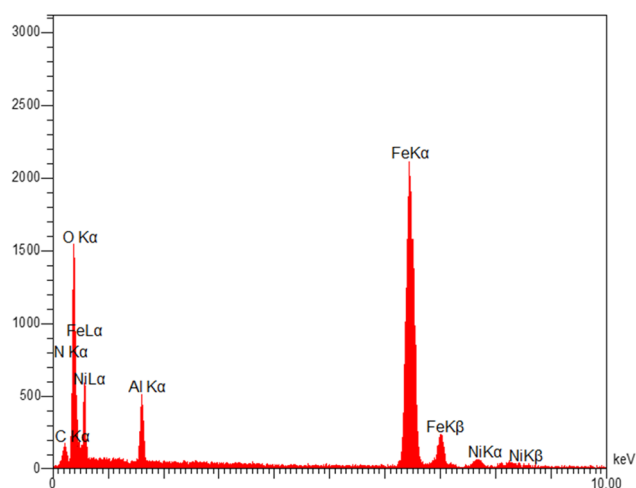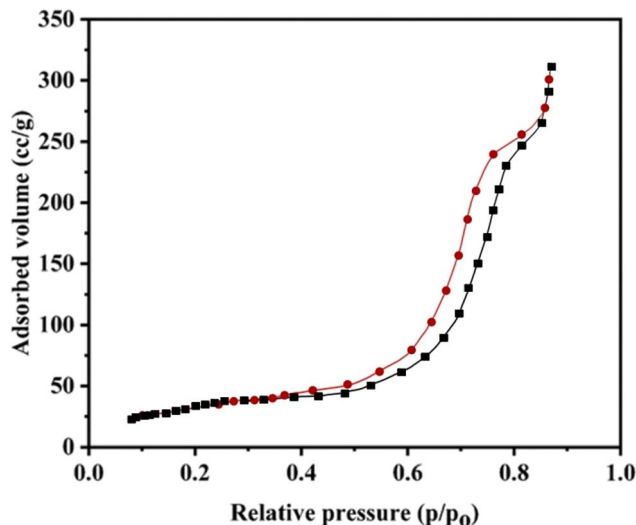

Fig. 3 EDX analysis of AlFe$_2$O$_4$@MWCNT–TEA–Ni(II) catalyst.

Fig. 4 BET analysis of AlFe$_2$O$_4$@MWCNT–TEA–Ni(II) nanocatalyst.

measured at around 5 nm, indicating that the pores are within a mesoporous range. This size facilitates diffusion processes during catalytic reactions, allowing for efficient transport of reactants and products.

The total pore volume is also determined to be about 0.35 cm^3 g^{-1}, further emphasizing the material's capacity to accommodate reactants within its porous structure. The combination of a high surface area, suitable pore diameter, and adequate pore volume suggests that this nanocatalyst is well-suited for enhancing reaction rates in various catalytic processes.

When comparing these characteristics with other catalysts reported in the literature, it becomes evident that AlFe$_2$O$_4$@MWCNT–TEA–Ni(II) stands out with its superior textural properties. These properties, including a high surface area and a suitable pore diameter, can enhance catalytic efficiency. While many conventional catalysts exhibit lower surface areas or larger pore diameters that may hinder mass transfer, this nanocatalyst's optimized structure allows for improved accessibility to active sites and better performance in catalytic reactions. Thus, these findings highlight the potential of AlFe$_2$O$_4$@MWCNT–TEA–Ni(II) and suggest exciting avenues for

future research to further improve catalyst design by manipulating textural properties.

Fig. 5 presents Scanning Electron Microscopy (SEM) and Transmission Electron Microscopy (TEM) images of the AlFe$_2$O$_4$@MWCNT–TEA–Ni(II) catalyst, showcasing its morphological characteristics at varying magnifications. The SEM image on the left reveals a rough surface texture, indicative of a porous structure that is likely beneficial for enhancing catalytic activity by increasing the available surface area for reactant interactions. The presence of aggregated particles suggests a high degree of interconnectivity among the nanomaterials, which can facilitate electron transfer processes critical in catalytic reactions.

In contrast, the TEM image on the right provides a more detailed view of the internal structure at a higher resolution. Here, individual nanoparticles are discernible, exhibiting sizes of approximately 10 to 50 nm. This nanoscale dimension is advantageous as it allows quantum effects to play a role in catalytic efficiency, potentially leading to improved reactivity compared to larger particles. The alignment of carbon nanotubes within the composite structure is also observable. These carbon nanotubes serve as a support matrix, providing a stable framework for the metal nanoparticles and as conduits for charge transport during catalytic processes, facilitating efficient electron transfer.

Comparative analysis of the SEM and TEM images highlights complementary aspects of the catalyst's morphology. While SEM provides insights into surface characteristics and overall particle distribution, TEM reveals finer structural details critical for understanding how these materials interact at a molecular level. Combining these imaging techniques underscores the significance of surface area and particle size in determining catalytic performance.

The observed morphology aligns well with existing literature on effective catalysts, where porous structures and nanoscale dimensions are often correlated with enhanced activity due to increased accessibility for reactants and improved mass transport. Furthermore, the integration of triethanolamine (TEA) plays a crucial role in stabilizing the metal nanoparticles within the composite, preventing agglomeration, and maintaining an optimal distribution essential for maximizing active sites.
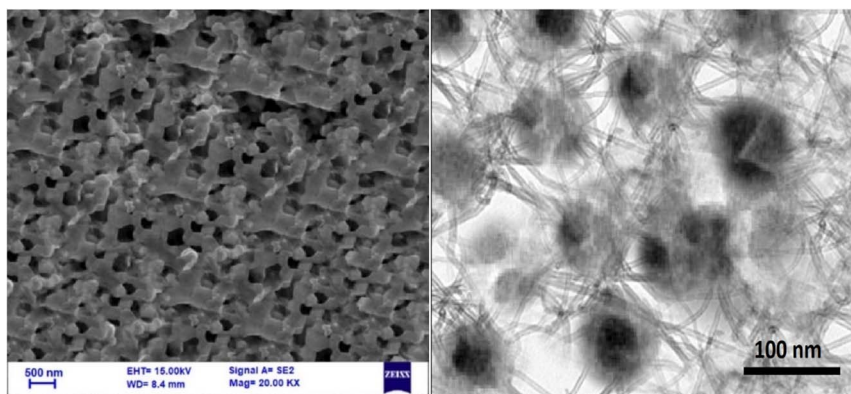

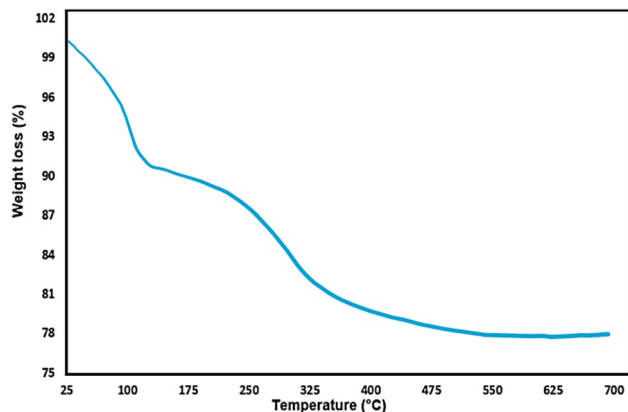Fig. 5 SEM and TEM images of AlFe$_2$O$_4$@MWCNT–TEA–Ni(II) catalyst at different magnifications.

Fig. 6 TGA of $AlFe_2O_4$@MWCNT–TEA–Ni(II) catalyst at different magnifications.

Fig. 5 illustrates how the structural features of $AlFe_2O_4$@-MWCNT–TEA–Ni(II) contribute to its potential efficacy as a catalyst. The synergistic effect between the metal oxide framework and carbon nanotube support enhances stability and promotes efficient electron transfer mechanisms. Future studies must investigate how these morphological characteristics influence specific catalytic activities across various reactions, thereby providing deeper insights into optimizing catalyst design for industrial applications.

Fig. 6 illustrates the Thermogravimetric Analysis (TGA) of the $AlFe_2O_4$@MWCNT–TEA–Ni(II) catalyst, depicting the relationship between weight loss and temperature across a range from 25 °C to 700 °C. The graph reveals a gradual decline in weight percentage, with significant weight loss occurring primarily within the initial temperature range up to approximately 175 °C. This initial drop can be attributed to the evaporation of moisture and the removal of any volatile organic compounds associated with the triethanolamine (TEA) used in synthesizing the catalyst.

As the temperature increases beyond 175 °C, a more gradual and steady weight loss is observed, which continues until around 400 °C. This phase likely corresponds to the decomposition of organic components and possibly some structural rearrangements within the composite material. The unique feature of the catalyst is the relatively stable region observed after this point, indicating that the inorganic framework of $AlFe_2O_4$ and MWCNTs remains intact, suggesting exceptional thermal stability of the catalyst under elevated temperatures.

The total weight loss recorded at temperatures approaching 700 °C is approximately 22%, indicating that a substantial portion of the mass is retained even at high temperatures. This retention suggests that the inorganic constituents provide significant structural integrity, crucial for maintaining catalytic activity during high-temperature reactions. The relatively low percentage of weight loss also implies minimal degradation or loss of active sites, which is an essential characteristic for catalysts intended for prolonged use in industrial applications.

When comparing these TGA results with similar studies on other metal oxide-based catalysts, it becomes evident that this composite exhibits favorable thermal stability characteristics. Many conventional catalysts often show higher rates of weight loss due to less stable organic components or poorly integrated structures. In contrast, the $AlFe_2O_4$@MWCNT–TEA–Ni(II) catalyst demonstrates a well-balanced composition that enhances its thermal properties and supports its potential efficacy in various catalytic processes, opening up exciting possibilities for its use in industrial applications.

TGA analysis provides critical insights into the thermal behavior and stability of the $AlFe_2O_4$@MWCNT–TEA–Ni(II) catalyst. The data indicate robust thermal resilience, vital for its application in catalytic reactions at elevated temperatures. Future investigations need to focus on correlating these thermal properties with specific catalytic performance metrics, which is a crucial aspect of the ongoing scientific inquiry, engaging the audience in the pursuit of further understanding of how such characteristics influence reaction efficiency and longevity in practical applications.

Fig. 7, a visual representation of the X-ray Diffraction (XRD) patterns of the $AlFe_2O_4$@MWCNT–TEA–Ni(II) catalyst alongside a reference pattern for Fe_2O_4, serves as a crucial tool for understanding the synthesized catalyst's crystalline structure and phase composition. The upper spectrum, corresponding to the $AlFe_2O_4$@MWCNT–TEA–Ni(II) composite, displays prominent diffraction peaks at specific 2-theta angles, indicating well-defined crystalline phases. The peak intensities suggest a high degree of crystallinity within the composite material, a key factor for its catalytic performance.

The most significant peaks appear around 30°, 35°, and 43°, aligning with standard values for $AlFe_2O_4$. This confirms the successful and precise incorporation of aluminum into the iron oxide framework. Additionally, these peaks suggest that the MWCNTs and TEA do not significantly alter the crystallinity of $AlFe_2O_4$ but serve as a supportive matrix that enhances overall stability and potentially facilitates electron transfer during catalytic processes.

In contrast, the lower spectrum representing Fe_2O_4 shows distinct peaks at similar 2-theta values but with lower intensity
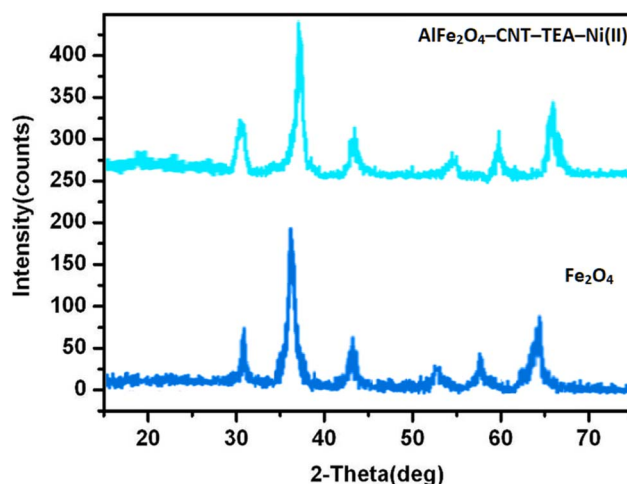

Fig. 7 XRD patterns of $AlFe_2O_4$@MWCNT–TEA–Ni(II) catalyst.

compared to those in the composite spectrum. This observation implies that while Fe_2O_4 is present in the catalyst formulation, its contribution to the overall crystallinity is less pronounced than that of $AlFe_2O_4$. The diminished intensity may also indicate that some degree of interaction occurs between Fe_2O_4 and other components in the composite, possibly leading to partial amorphization or solid solution formation. These interactions could alter the catalyst's reactivity and stability, which should be further investigated.

Comparatively analyzing both spectra reveals critical insights into how the structural characteristics of these materials influence their potential catalytic applications. The enhanced peak intensities and sharper diffraction patterns observed in the $AlFe_2O_4$@MWCNT–TEA–Ni(II) catalyst suggest improved stability and reactivity due to better-defined crystalline structures. This contrasts with conventional catalysts, where broader peaks often signify lower crystallinity and less effective active sites.

Furthermore, this study's findings align with existing literature on metal oxide catalysts, where higher crystallinity is frequently associated with increased catalytic activity due to more accessible active sites and improved mass transport properties. The integration of MWCNTs within this composite contributes to structural integrity and may enhance electronic conductivity, further augmenting catalytic efficiency.

Fig. 7 effectively illustrates the crystalline nature of the $AlFe_2O_4$@MWCNT–TEA–Ni(II) catalyst compared to Fe_2O_4 alone. The XRD patterns underscore the importance of structural composition in determining catalytic performance. This study's findings, which align with existing literature on metal oxide catalysts, suggest that the $AlFe_2O_4$@MWCNT–TEA–Ni(II) catalyst holds significant potential for industrial applications. Future research should aim to correlate these structural features with specific catalytic activities across various reactions to fully understand how such characteristics can be optimized for such applications.

Fig. 8 presents the Vibrating Sample Magnetometry (VSM) spectra for $AlFe_2O_4$ nanoparticles (NPs) and the $AlFe_2O_4$–MWCNT–TEA–Ni(II) catalyst, highlighting their magnetic properties as a function of the applied magnetic field. The graph illustrates the magnetization (in emu g^{-1}) plotted against the

magnetic field (in Oe), revealing distinct characteristics of each material's magnetic behavior.

The VSM spectrum for $AlFe_2O_4$ NPs, represented by the dashed blue line, exhibits a clear hysteresis loop, indicative of ferromagnetic behavior. This loop demonstrates that the material retains a significant amount of magnetization even after removing the external magnetic field, which is a desirable property for applications in magnetic separation and catalysis. The maximum magnetization observed for $AlFe_2O_4$ NPs reaches approximately 70 emu g^{-1} at high magnetic fields, reflecting strong ferromagnetic interactions within the nanoparticle assembly.

In contrast, the red dashed line representing the $AlFe_2O_4$–MWCNT–TEA–Ni(II) catalyst shows a notable difference in its magnetic response. While this composite also displays ferromagnetic characteristics, its maximum magnetization is lower than that of pure $AlFe_2O_4$ NPs, peaking around 55 emu g^{-1}. The reduced magnetization can be attributed to several factors, including possible dilution effects due to the incorporation of multi-walled carbon nanotubes (MWCNTs) and triethanolamine (TEA), which may disrupt the dense packing of iron oxide particles and alter their magnetic interactions. This reduction in magnetization, however, is accompanied by other beneficial properties, such as increased responsiveness to external magnetic fields, which can facilitate easier recovery and reusability of the catalyst in practical applications.

Furthermore, the shape of the composite's hysteresis loop indicates a shift towards superparamagnetic behavior at lower fields. This transition suggests that while the composite retains some ferromagnetic properties, it may exhibit enhanced responsiveness to external magnetic fields. This enhanced responsiveness, attributed to factors such as reduced particle size or increased surface area resulting from MWCNT integration, allows the catalyst to be more easily manipulated and recovered using magnetic fields. Such characteristics facilitate easier recovery and reusability of the catalyst in practical applications, enhancing its operational efficiency and ease of use.

Comparative analysis of these results reveals significant insights into how structural modifications influence magnetic properties. The presence of MWCNTs contributes to mechanical stability and affects the catalyst's overall magnetic response. This finding aligns with existing literature that reports similar observations where hybrid materials exhibit altered magnetic behaviors compared to their pure counterparts.

Fig. 8 effectively highlights the differences in magnetic properties between $AlFe_2O_4$ NPs and the $AlFe_2O_4$–MWCNT–TEA–Ni(II) catalyst. The data suggest that while both materials possess ferromagnetic characteristics, modifications through composite formation lead to changes in magnetization levels and hysteresis behavior. These findings underscore the potential advantages of utilizing such composites in catalytic applications where thermal stability and magnetic responsiveness are crucial for operational efficiency and ease of recovery. This opens up intriguing possibilities for future studies to investigate how these magnetic properties correlate with catalytic
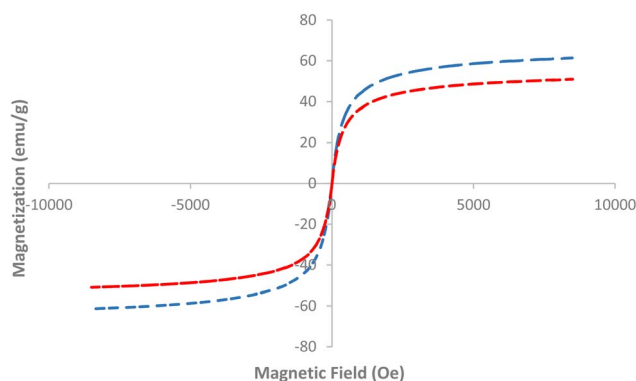

Fig. 8 VSM spectrums of $AlFe_2O_4$ NPs and $AlFe_2O_4$–MWCNT–TEA–Ni(II) catalyst.
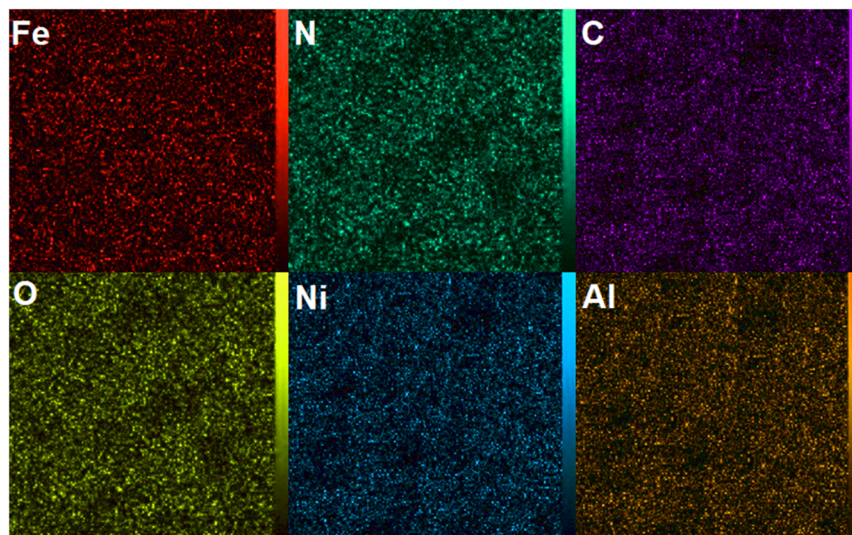
Fig. 9 Elemental mapping AlFe$_2$O$_4$–MWCNT–TEA–Ni(II) nanocatalyst.

performance across various reactions, optimizing their application in industrial processes.

Fig. 9 presents the elemental mapping of the AlFe$_2$O$_4$–MWCNT–TEA–Ni(II) nanocatalyst, providing a comprehensive visualization of the spatial distribution of key elements within the composite material. The mapping includes iron (Fe), nitrogen (N), carbon (C), oxygen (O), nickel (Ni), and aluminum (Al), each represented in distinct colors. This allows for an intuitive understanding of the elemental composition and uniformity across the catalyst.

The red channel indicates a significant presence of iron, which is expected given that AlFe$_2$O$_4$ serves as a primary component of the catalyst. The uniform distribution of iron throughout the mapped area suggests that it is well-integrated within the composite structure, instilling confidence in the catalyst's structural integrity. This is crucial for maintaining the catalytic activity associated with iron oxides.

In the green channel, nitrogen appears prominently, indicating its successful incorporation into the catalyst framework through triethanolamine (TEA). This incorporation may play a vital role in enhancing the stability and dispersion of metal species within the composite, potentially influencing catalytic performance by facilitating better interaction between active sites and reactants.

The carbon mapping, shown in purple, reveals a consistent presence of carbon throughout the sample, attributed to including multi-walled carbon nanotubes (MWCNTs). The even distribution of carbon supports structural integrity and enhances electronic conductivity, providing a sense of security about the catalyst's ability to facilitate efficient electron transfer in catalytic reactions.

Oxygen is represented in yellow and widespread across the mapped area. This finding aligns with expectations since oxygen is integral to both AlFe$_2$O$_4$ and various functional groups present in TEA. Oxygen is essential for maintaining the oxidative states necessary for catalytic processes.

Nickel, depicted in blue, demonstrates a uniform distribution within the composite. Incorporating nickel ions into this nanocatalyst is critical as it enhances catalytic activity through synergistic effects with iron oxides. The even dispersion of nickel suggests effective interaction with other components, which can lead to improved overall performance in catalytic applications.

Finally, aluminum is shown in orange, confirming its presence as part of AlFe$_2$O$_4$. The mapping indicates that aluminum is uniformly distributed alongside iron and oxygen, reinforcing its role in stabilizing the ferrite structure while potentially enhancing catalytic efficiency.

Comparative analysis of these elemental distributions highlights several important aspects regarding the synthesis and functionality of the AlFe$_2$O$_4$–MWCNT–TEA–Ni(II) catalyst. The uniformity observed across all elements suggests that each component has been effectively integrated during synthesis, which is vital for achieving optimal catalytic properties. Furthermore, this homogeneous distribution may enhance interactions among active sites within the catalyst matrix, promoting more efficient reaction pathways.

Fig. 9 provides valuable insights into the elemental composition and spatial arrangement within the AlFe$_2$O$_4$–MWCNT–TEA–Ni(II) nanocatalyst. The successful integration of key elements such as iron, nitrogen, carbon, oxygen, nickel, and aluminum underscores the effectiveness of the synthesis process, providing a sense of reassurance. It sets a foundation for further exploration into how these structural attributes influence catalytic behavior. Future investigations should focus on correlating these elemental mappings with specific catalytic activities to optimize performance across various chemical reactions.

Reusability and stability of the catalyst

Fig. 10 illustrates the reusability of the AlFe$_2$O$_4$–MWCNT–TEA–Ni(II) catalyst in the synthesis of 5-phenyl-1H-tetrazole (**3a**) over seven consecutive experimental runs, each conducted under [specific conditions]. The isolated yields, represented as
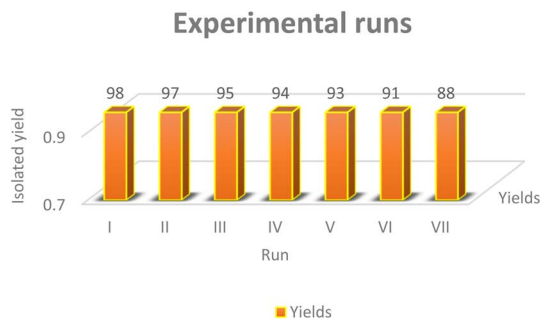
Experimental runs

Fig. 10 Reusability of $AlFe_2O_4$–MWCNT–TEA–Ni(II) as a catalyst for synthesizing 5-phenyl-1H-tetrazole (**3a**).

Fig. 11 After seven runs, the FT-IR spectra between the fresh and reused catalysts were compared.

a percentage on the vertical axis, demonstrate a gradual decline in catalytic performance with each subsequent run, starting from an impressive yield of 98% in the first run and decreasing to 88% by the seventh run.

The data indicates that the catalyst maintains high efficiency throughout its initial applications, with yields above 90% for the first five runs. This consistent performance suggests that the $AlFe_2O_4$–MWCNT–TEA–Ni(II) catalyst exhibits excellent stability and effectiveness during the early stages of use, likely due to its well-integrated structure and favorable interaction between its components. While not significant, the slight decrease in yield from 98% to 97% in the second run is important as it indicates minimal activity loss and suggests that the catalyst is robust and can be used multiple times without a substantial decrease in performance.

However, a more pronounced decline is observed in runs six and seven, where yields drop to 91% and 88%, respectively. This reduction may be attributed to several factors, including potential leaching of active metal species, deactivation of catalytic sites, or aggregation of nanoparticles over repeated use. Such phenomena are common in heterogeneous catalysis and underscore the importance of understanding catalyst longevity and performance degradation mechanisms. This understanding is crucial for the development of more durable and efficient catalysts.

Comparative analysis of these results provides insight into the efficacy and limitations of the $AlFe_2O_4$–MWCNT–TEA–Ni(II) catalyst. While it demonstrates remarkable initial performance, the gradual decline in yield raises questions regarding its long-term viability for industrial applications. The observed trend emphasizes the need for further optimization strategies to enhance catalyst durability. This could involve modifications to improve metal anchoring within the composite or exploring alternative support materials that may mitigate leaching effects.

Fig. 10 effectively showcases the reusability profile of the $AlFe_2O_4$–MWCNT–TEA–Ni(II) catalyst for synthesizing 5-phenyl-1H-tetrazole (**3a**). The initial high yields underscore its potential as a robust catalytic system; however, the declining yields across multiple runs highlight critical areas for future research focused on enhancing stability and reactivity over extended periods. Further investigations should aim to elucidate the underlying causes of yield reduction and explore methods to
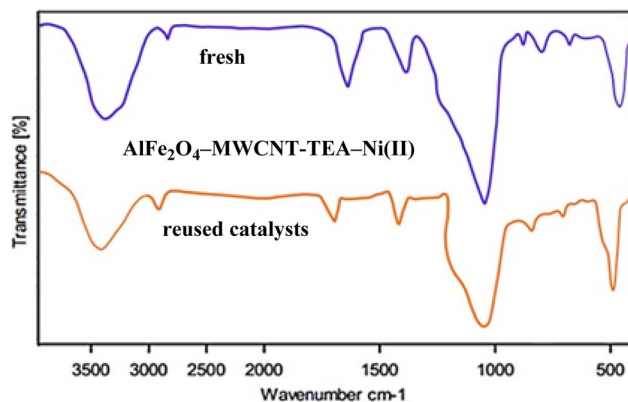
sustain catalytic performance throughout prolonged usage cycles.

Fig. 11 presents a comparative analysis of the Fourier Transform Infrared (FT-IR) spectra of the $AlFe_2O_4$–MWCNT–TEA–Ni(II) catalyst in its fresh state and after seven consecutive catalytic runs. The spectral data, plotted with transmittance percentage on the vertical axis against wavenumber (cm^{-1}) on the horizontal axis, provides insights into the catalyst's structural integrity and chemical environment before and after use.

The FT-IR spectrum for the fresh catalyst, represented in blue, exhibits characteristic peaks that correspond to various functional groups within the composite material. Notably, strong absorption bands are observed in the regions around $3400~cm^{-1}$, which can be attributed to O–H stretching vibrations from hydroxyl groups, and around $1620~cm^{-1}$, indicative of C=O stretching associated with carbonyl functionalities. Additionally, peaks below $1000~cm^{-1}$ suggest the presence of metal–oxygen bonds typical of iron and aluminum oxides.

In contrast, the spectrum for the reused catalyst, shown in orange, reveals several notable differences. A decrease in intensity for the O–H stretching band at approximately $3400~cm^{-1}$ suggests a reduction in hydroxyl groups or changes in their hydrogen bonding environment due to repeated catalytic activity. Furthermore, shifts or broadening of peaks in the carbonyl region may indicate alterations in surface chemistry or interactions between active sites and reactants during catalysis. The lower transmittance values observed across various wavenumbers imply that some structural modifications have occurred due to prolonged use.

Comparative analysis of these spectra indicates that while the fundamental structure of the $AlFe_2O_4$–MWCNT–TEA–Ni(II) catalyst remains intact after seven runs, there are significant changes in its surface chemistry and functional group availability. These alterations, such as the decrease in O–H stretching band intensity and shifts in the carbonyl region, could account for the observed decline in catalytic performance. Specifically, changes in active site accessibility or alterations to electronic properties may hinder efficient interaction with substrates, leading to reduced catalytic activity.
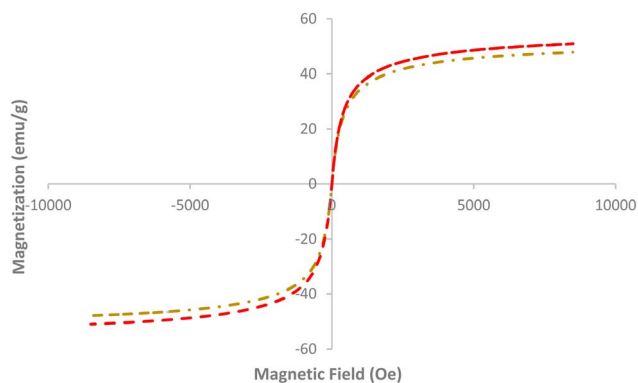
Fig. 12 VSM images of AlFe$_2$O$_4$–MWCNT–TEA–Ni(II) catalyst reused catalyst after seven runs.

Fig. 11 vividly demonstrates the power of FT-IR spectroscopy in tracking changes in chemical structure and functionality within catalysts over time. The disparities between fresh and reused catalysts underscore crucial aspects of catalyst deactivation mechanisms and pinpoint areas for further exploration to enhance stability and reusability. Future studies should concentrate on establishing a correlation between these spectral changes and specific catalytic activities, thereby providing a deeper understanding of how molecular modifications influence overall performance during extended usage cycles.

Fig. 12 presents the Vibrating Sample Magnetometry (VSM) analysis of the AlFe$_2$O$_4$–MWCNT–TEA–Ni(II) catalyst after seven consecutive catalytic runs. The graph plots magnetization (emu g^{-1}) on the vertical axis against the magnetic field (Oe) on the horizontal axis, providing insights into the reused catalyst's magnetic properties.

The VSM data indicates a characteristic hysteresis loop, typical for ferromagnetic materials. This loop suggests that the catalyst retains significant magnetic properties even after multiple cycles of catalytic activity. Notably, as the magnetic field increases from hostile to positive values, there is a corresponding increase in magnetization, reaching a saturation point at approximately 50 emu g^{-1}. This saturation magnetization reflects the effective alignment of magnetic moments within the material under an external magnetic field.

Upon analyzing the graph, it becomes evident that there is minimal change in the shape and magnitude of the hysteresis loop when comparing data from fresh and reused catalysts. This stability in magnetic properties implies that the structural integrity of the AlFe$_2$O$_4$ component remains intact mainly despite repeated use in catalytic reactions. The consistent saturation magnetization suggests that any potential degradation or alteration in physical structure due to catalytic activity does not significantly impact its magnetic characteristics.

Furthermore, comparing these results with previous findings regarding catalytic performance reveals an interesting correlation. While there was a noted decline in catalytic efficiency after multiple runs, as illustrated in earlier figures, this decline is not directly linked to a loss of magnetic properties. Instead, it may be more closely associated with changes in surface chemistry or
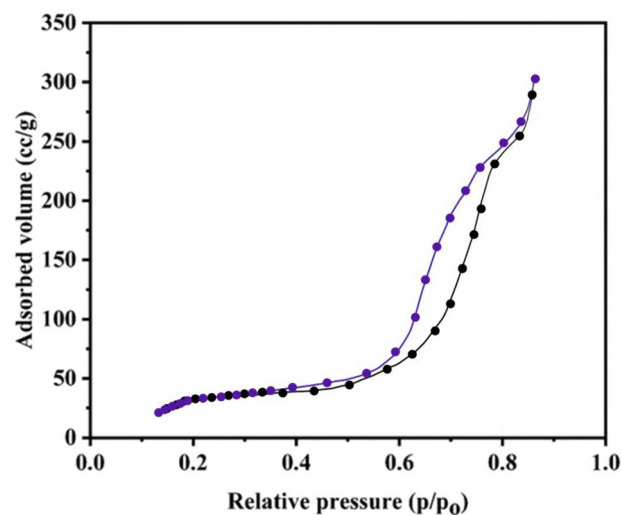

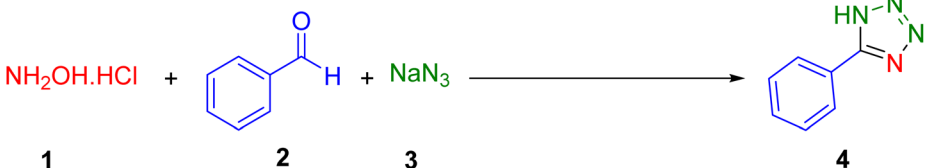**Fig. 13** BET images of AlFe$_2$O$_4$–MWCNT–TEA–Ni(II) catalyst reused catalyst after seven runs.

active site availability rather than structural degradation of the magnetic framework itself.

Fig. 12 underscores the robustness of the AlFe$_2$O$_4$–MWCNT–TEA–Ni(II) catalyst's magnetic properties even after extensive use in catalysis. Retaining significant magnetization highlights its potential for easy recovery and reuse in practical applications. However, while magnetism remains stable, further investigation is warranted to explore how changes at the molecular level during catalysis affect overall performance and reactivity. Future studies should aim to dissect these relationships more thoroughly to enhance our understanding of catalyst behavior over extended operational periods.

Fig. 13 presents a crucial analysis of the Brunauer–Emmett–Teller (BET) adsorption isotherm of the AlFe$_2$O$_4$–MWCNT–TEA–Ni(II) catalyst after seven consecutive catalytic runs. This graph, which plots the adsorbed volume (cm^3 g^{-1}) against the relative pressure (p/p_0), is a key tool in understanding the reused catalyst's surface area and porosity characteristics.

The BET isotherm reveals a type IV adsorption behavior indicative of mesoporous materials. This is evident from the gradual increase in adsorbed volume with rising relative pressure, particularly in the range of 0.3 to 0.8 p/p_0, where a significant rise in adsorption occurs. The plateau observed at higher pressures suggests that most of the available pore volume has been filled, reflecting a well-developed porous structure conducive to catalytic activity.

Upon comparing the data represented by the black and purple curves, it becomes clear that there are subtle differences in adsorption behavior between two measurements taken after seven runs. The black curve represents one set of measurements while the purple curve indicates another; both exhibit similar trends but differ slightly in adsorbed volume at specific relative pressures. Notably, at lower relative pressures (below 0.4 p/p_0), there is a marked increase in adsorbed volume for the purple curve compared to the black curve, suggesting enhanced accessibility or availability of surface area for gas adsorption after repeated catalytic use.

Table 1 Evaluation of the reaction parameter on the synthesis of 5-phenyl-1H-tetrazole over the catalysis of AlFe$_2$O$_4$–MWCNT–TEA–Ni(II)

Entry	Catalyst	Catalyst (mg)	Solvent^b	Temperature (°C)	Time (min)	Yield^a (%)
1	—	—	DMF	70	600	—
2	FeCl$_2$·4H$_2$O	5	DMF	50	60	—
3	Al(NO$_3$)$_3$·9H$_2$O	5	DMF	50	60	—
4	Ni(NO$_3$)$_2$·6H$_2$O	5	DMF	50	60	—
5	AlFe$_2$O$_4$ NPS	5	DMF	50	60	19
6	AlFe$_2$O$_4$@MWCNT	5	DMF	50	60	27
7	AlFe$_2$O$_4$–MWCNT–TEA	5	DMF	50	60	38
8	AlFe$_2$O$_4$–MWCNT–TEA–Ni(II)	5	DMF	RT	600	47
9	**AlFe$_2$O$_4$–MWCNT–TEA–Ni(II)**	**5**	**DMF**	**50**	**60**	**98**
10	AlFe$_2$O$_4$–MWCNT–TEA–Ni(II)	5	DMF	70	60	96
11	AlFe$_2$O$_4$–MWCNT–TEA–Ni(II)	10	DMF	50	60	95
12	AlFe$_2$O$_4$–MWCNT–TEA–Ni(II)	5	CH$_3$CN	50	60	46
13	AlFe$_2$O$_4$–MWCNT–TEA–Ni(II)	5	CH$_3$Cl	50	60	38
14	AlFe$_2$O$_4$–MWCNT–TEA–Ni(II)	5	MeOH	50	60	45
15	AlFe$_2$O$_4$–MWCNT–TEA–Ni(II)	5	EtOH	50	60	49
16	AlFe$_2$O$_4$–MWCNT–TEA–Ni(II)	5	H$_2$O	50	60	53
17	AlFe$_2$O$_4$–MWCNT–TEA–Ni(II)	5	CH$_2$Cl$_2$	50	60	35

^{a} Isolated yield. ^{b} Conditions: benzaldehyde (1 mmol), hydroxylamine (1.2 mmol), and sodium azide (1.3 mmol), catalyst (mg) and solvent (1 mL).

This observation raises important questions regarding changes in pore structure or surface chemistry that may have occurred during catalysis. It implies that while some active sites may have been blocked or altered due to reaction byproducts or structural changes, others may have become more accessible or reactive due to these interactions. Such dynamics could explain variations in catalytic performance noted previously, where specific active sites were rendered less effective. In contrast, others became more favorable for reactions, potentially leading to significant improvements in catalyst performance.

Fig. 13 provides valuable insights into how repeated usage affects the porosity and surface characteristics of the AlFe$_2$O$_4$–MWCNT–TEA–Ni(II) catalyst. Retaining mesoporosity alongside adsorption capacity variations highlights resilience and adaptability within its structural framework after multiple catalytic runs. This underscores the need for future studies to focus on further elucidating these changes to optimize catalyst design and enhance performance through targeted modifications to maximize active site accessibility and reactivity over extended operational periods.

The synthesis of 5-phenyl-1H-tetrazole from benzaldehyde, hydroxylamine hydrochloride, and sodium azide was investigated using various catalytic systems (Table 1). The reaction optimization focused on identifying the most effective catalyst, solvent, temperature, and reaction time.

Initial experiments explored the use of metal salts such as FeCl$_2$·4H$_2$O, Al(NO$_3$)$_3$·9H$_2$O, and Ni(NO$_3$)$_2$·6H$_2$O (entries 2–4), but these proved ineffective under the tested conditions (50 °C,

60 min, DMF). Subsequently, the catalytic activity of AlFe$_2$O$_4$ nanoparticles (NPs) and AlFe$_2$O$_4$@MWCNT was evaluated (entries 5 and 6), yielding only modest conversions (19% and 27%, respectively).

Significant improvement was observed upon incorporating triethylamine (TEA) and Ni(II) into the catalytic system, forming AlFe$_2$O$_4$–MWCNT–TEA–Ni(II). This catalyst demonstrated superior performance, achieving a 38% yield under the standard conditions (entry 7). Further optimization revealed that increasing the reaction time to 600 min at room temperature with AlFe$_2$O$_4$–MWCNT–TEA–Ni(II) yielded a 47% yield (entry 8). The most effective conditions were identified as using AlFe$_2$O$_4$–MWCNT–TEA–Ni(II) (5 mg) in DMF at 50 °C for 60 min, affording the desired 5-phenyl-1H-tetrazole in an excellent yield of 98% (entry 9). Increasing the temperature to 70 °C did not improve the yield (96%, entry 10). Doubling the catalyst loading to 10 mg did not significantly improve the yield (95%, entry 11), indicating 5 mg is the optimal amount.

The influence of the solvent was also investigated. While DMF proved to be the optimal solvent, other solvents were screened. Acetonitrile (CH$_3$CN) provided a 46% yield, dichloromethane (CH$_2$Cl$_2$) a 35% yield, methanol (MeOH) a 45% yield, ethanol (EtOH) a 49% yield, and water (H$_2$O) a 53% yield (entries 12–17). These results highlight the crucial role of DMF in achieving high yields, likely due to its polarity and ability to effectively solvate the reactants and catalyst.

In summary, the optimized conditions for the synthesis of 5-phenyl-1H-tetrazole involve using AlFe$_2$O$_4$–MWCNT–TEA–Ni(II)
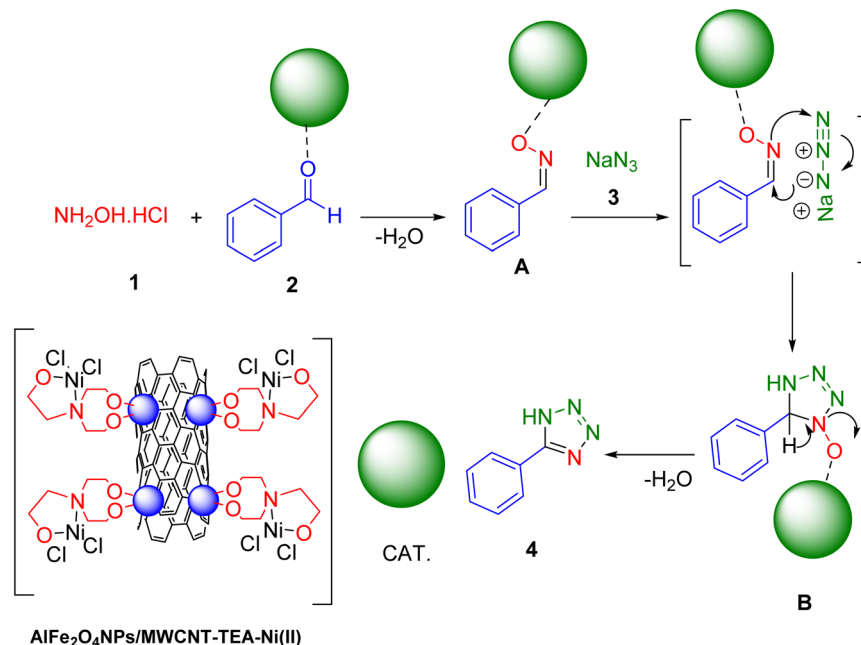
Scheme 3 A plausible mechanism for the click synthesis of 5-aryl-1*H*-tetrazoles over the catalysis of AlFe$_2$O$_4$–MWCNT–TEA–Ni(II).

(5 mg) as the catalyst in DMF (1 mL) at 50 °C for 60 min using benzaldehyde (1 mmol), hydroxylamine hydrochloride (1.2 mmol), and sodium azide (1.3 mmol). These conditions provide an efficient and high-yielding route to the desired tetrazole product.

The Scheme 3 illustrates a plausible mechanism for synthesizing 5-aryl-1*H*-tetrazoles using a catalyst denoted as AlFe$_2$O$_4$–MWCNT–TEA–Ni(II). The starting materials are hydroxylamine hydrochloride (**1**) and aryl amine (**2**). In the presence of acid, hydroxylamine hydrochloride reacts with the aryl amine to form a diazonium salt (**A**). This is a classic diazotization reaction. The diazonium salt (**A**) coordinates with the nickel center (Ni(II)) of the catalyst (AlFe$_2$O$_4$–MWCNT–TEA–Ni(II)). The catalyst likely provides a surface for the reaction to occur. Sodium azide (NaN$_3$) acts as a nucleophile. The azide ion attacks the carbon atom of the diazonium group, leading to the formation of a tetrazole intermediate (**B**). A proton transfer occurs, likely involving the catalyst or solvent, resulting in the final product, 5-aryl-1*H*-tetrazole (**4**).

The catalyst (AlFe$_2$O$_4$–MWCNT–TEA–Ni(II)) plays a crucial role in this reaction:

Surface for reaction: it provides a surface for the reactants to adsorb and react. This can increase the effective concentration of the reactants and enhance the reaction rate.

Stabilization of intermediates: the catalyst might stabilize the intermediate species formed during the reaction, preventing their decomposition.

Activation of reactants: the nickel center in the catalyst could activate the diazonium salt, making it more susceptible to nucleophilic attack by the azide ion.

Table 2 presents the results from a comprehensive study aimed at synthesizing 5-substituted-1*H*-tetrazoles utilizing the catalyst AlFe$_2$O$_4$–MCNT–TEA–Ni(II). In this investigation,

various aldehydes (denoted as **2**) were employed in the presence of the specified catalyst to facilitate the reactions.

The data in Table 2 illustrates that the reactions encompassed a diverse range of aldehydes, which included both those with electron-donating substituents and those with electron-withdrawing substituents. Notably, all substrates yielded high amounts of the desired tetrazole products, indicating the effectiveness of the catalyst in promoting these transformations.

However, a significant observation was that aldehydes featuring electron-donating substituents necessitated longer reaction times. This phenomenon can be attributed to the diminished electrophilic character of their carbonyl groups, which slows down the reaction rate. In contrast, aldehydes with electron-withdrawing substituents tended to react more swiftly, likely due to their increased electrophilicity, facilitating a more efficient reaction process.

Moreover, the study highlighted the impact of steric effects on the reaction outcomes. Steric hindrance from bulky substituents can impede the approach of the reactants, thereby influencing both the reaction rate and yield of the final products. This aspect underscores the importance of considering both electronic and steric factors when optimizing conditions for the synthesis of 5-substituted 1*H*-tetrazoles. Overall, the findings suggest that while the AlFe$_2$O$_4$–MCNT–TEA–Ni(II) catalyst is effective across a range of substrates, the nature of the substituents on the aldehydes plays a crucial role in determining the efficiency and duration of the reactions.

Table 3 compares various catalysts for the model reaction of 5-aryl-1*H*-tetrazole (**4a**) synthesis. The table highlights the catalyst, reaction conditions, time required, and product yield. The AlFe$_2$O$_4$–MWCNT–TEA–Ni(II) catalyst demonstrates exceptional efficiency, achieving a 98% yield in just 1 minute at

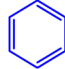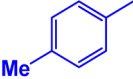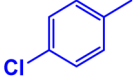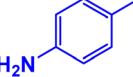**Table 2** The synthesis of 5-substituted 1*H*-tetrazoles over the catalysis of AlFe$_2$O$_4$–MWCNT–TEA–Ni(II)
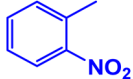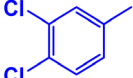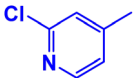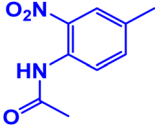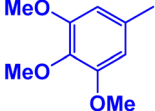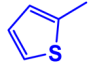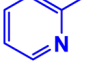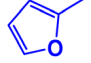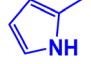
$$\text{NH}_2\text{OH.HCl} + \underset{2}{\text{Ar}-\text{CHO}} + \underset{3}{\text{NaN}_3} \xrightarrow[\text{DMF, 50 °C}]{\text{AlFe}_2\text{O}_4-\text{MWCNT}-\text{TEA}-\text{Ni(II)}} \underset{4}{\text{Ar}-\text{tetrazole}}$$

Entry	R	Time (min)	Yield (%)	M.p. °C	M.p. °C [ref.]
1	phenyl	60	98	213–215	214–216 (ref. 67)
2	4-Me, 2-Me phenyl	75	95	246–248	247–249 (ref. 68)
3	4-Cl phenyl	70	93	259–261	258–260 (ref. 69)
4	4-H$_2$N phenyl	80	92	264–266	264–266 (ref. 70)
5	2-NO$_2$ phenyl	50	91	155–157	156–158 (ref. 69)
6	HO, Br phenyl	70	92	173–175	171–173 (ref. 71)
7	2,3-diCl phenyl	80	93	148–150	148–150 (ref. 72)
8	2-Cl pyridinyl	85	95	198–200	200–202 (ref. 72)
9	O$_2$N, HN-C(O)CH$_3$ phenyl	55	94	210–212	212–214 (ref. 73)
10	MeO, MeO, OMe phenyl	80	90	200–202	201–203 (ref. 73)
11	thienyl	50	92	201–203	200–202 (ref. 69)
12	pyridinyl	65	94	210–212	210–212 (ref. 74)
13	furyl	60	94	201–203	200–202 (ref. 75)
14	pyrrolyl	70	90	224–226	224–226 (ref. 74)

Table 2 (*Contd.*)

$$NH_2OH \cdot HCl + \underset{2}{Ar\text{-}CHO} + \underset{3}{NaN_3} \xrightarrow[\text{DMF, 50 °C}]{\text{AlFe}_2\text{O}_4\text{–MWCNT–TEA–Ni(II)}} \underset{4}{Ar\text{-tetrazole}}$$

Entry	R	Time (min)	Yield (%)	M.p. °C	M.p. °C [ref.]
15	5-methylpyrimidine	70	91	253–255	252–254 (ref. 70)
16	2-methylnaphthalene	70	90	202–204	203–205 (ref. 69)
17	2-(4-nitrophenyl)-5-methyl-1H-benzimidazole	85	89	276–278	275–277 (ref. 68)
18	1-methylisoquinoline	75	90	235–237	235–237 (ref. 70)

a relatively low temperature of 50 °C. This is significantly faster and more efficient than most other catalysts listed. The reaction temperature appears to play a crucial role. Catalysts requiring higher temperatures generally take longer to complete the reaction. For instance, Cu-MCM-41-DMF requires 140 °C and 12 minutes, while Fe_3O_4–MWCNT–TEA–Cu(ɪɪ) operates at 70 °C for 1.5 minutes. The table showcases various catalysts, including metal-based, metal oxide-based, and supported catalysts. This diversity underscores the ongoing research efforts to identify optimal catalysts for this reaction. $AlFe_2O_4$–MWCNT–TEA–Ni(ɪɪ) stands out as the most efficient catalyst in terms of both reaction time and yield. It outperforms established catalysts like Cu-MCM-41-DMF and $Bi(OTf)_3$-DMF regarding reaction time and yield. The low reaction temperature of 50 °C for $AlFe_2O_4$–MWCNT–TEA–Ni(ɪɪ) is particularly noteworthy. This reduces

energy consumption and minimizes potential side reactions or catalyst degradation that might occur at higher temperatures. Overall, the $AlFe_2O_4$–MWCNT–TEA–Ni(ɪɪ) catalyst demonstrates promising potential for synthesizing 5-aryl-1*H*-tetrazoles. Its high activity, low reaction temperature, and rapid reaction time make it a compelling alternative to existing catalysts.

Leaching (hot filtration test)

Fig. 14 presents the results of a leaching experiment conducted to evaluate the catalytic performance of $AlFe_2O_4$–MWCNT–TEA–Ni(ɪɪ) under hot filtration conditions. The graph illustrates the yield percentages over time, comparing two scenarios: one where the catalyst remains in the reaction mixture (represented by the orange line) and another where the catalyst is filtered out after a specific time point (indicated by the blue line).

Table 3 Comparison of catalytic efficiency of $AlFe_2O_4$–MWCNT–TEA–Ni(ɪɪ) in the model reaction of synthesis of 5-aryl-1*H*-tetrazole (**3a**)

Entry	Conditions	Time (h)	Yield (%)	Ref.
1	$InCl_3$[a] (3 mol%)-DMF-120 °C	15	92	67
2	Cu-MCM-41 (5 mol%)-DMF-140 °C	12	90	68
3	$((NH_4)CeSO_4)_4$–$2H_2O$ (20 mol%)-DMF-reflux	5	72	69
4	$Bi(OTf)_3$-DMF(5 mol%)-120 °C	24	87	70
5	$Cu(OAc)_2$[a] (25 mol%)-DMF-120 °C	12	98	71
6	$Cu(OAc)_2$ (20 mol%)-DMF-120 °C	12	96	72
7	Nano-Cu_2O-MFR[b] (0.3 g)-DMF-100 °C	8	92	73
8	P_2O_5 (4 mol%)-DMF-reflux	4	90	74
9	Fe_3O_4–MWCNT–TEA–Cu(ɪɪ) (5 mg)-DMF-70 °C	1.5	96	75
10	**$AlFe_2O_4$–MWCNT–TEA–Ni(ɪɪ) (5 mg)-DMF-50 °C**	**1**	**98**	**This study**

[a] The substrate is benzaldoxime. [b] Melamine–formaldehyde resin.

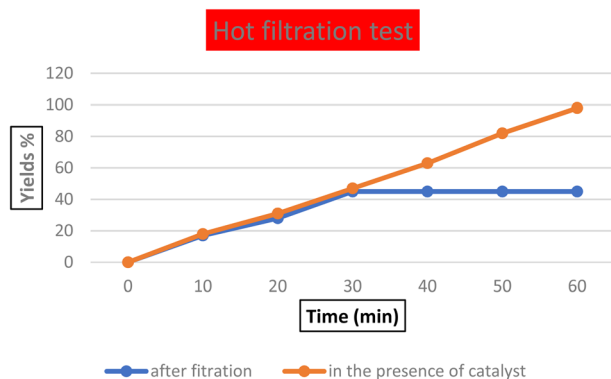**Fig. 14** Leaching experiment of $AlFe_2O_4$–MWCNT–TEA–Ni(II).

The data reveal that there is a steady increase in yield percentages in the presence of the catalyst, reaching nearly 100% by the end of the 60-minute reaction period. This suggests that the catalyst effectively facilitates the reaction, enhancing product formation throughout the experiment. Conversely, after filtration, there is a marked decrease in yield progression; while some product formation occurs initially, it plateaus at around 40%. This significant drop indicates that once the catalyst is removed from the reaction medium, its ability to promote further reactions diminishes substantially.

The comparative analysis of these two scenarios underscores the critical role of the $AlFe_2O_4$–MWCNT–TEA–Ni(II) catalyst in sustaining high yields during catalytic reactions. The initial yield observed after filtration suggests that some products can be formed without continuous catalytic action; however, this is insufficient for achieving optimal yields. The stark contrast between both lines not only underscores the effectiveness of this particular catalyst but also emphasizes the urgency of continuous catalytic involvement for achieving optimal yields. This highlights the necessity of our research in the field of catalysis and the potential impact it can have on practical applications.

These findings underscore the importance of catalyst retention in heterogeneous catalysis processes. The results indicate that while some reactions may occur without an active catalyst present, significant enhancements in yield are only achievable through continuous catalytic involvement. Thus, strategies aimed at minimizing catalyst loss during reactions could further improve overall efficiency and productivity in practical applications involving $AlFe_2O_4$–MWCNT–TEA–Ni(II).

Experimental

Materials and methods

This research used materials obtained from Merck and Aldrich without any further purification. Carboxylated multiwall carbon nanotubes with specific physical characteristics were sourced from Aldrich. The concentration of Fe_3O_4 nanoparticles was analyzed using an inductively coupled plasma optical emission spectrometer, and scanning and transmission electron microscopy provided detailed images of the materials. Dynamic

light scattering was employed to evaluate the nanoparticle size, and thermogravimetric analysis was conducted in a nitrogen atmosphere to assess thermal stability. Melting points were determined using an Electrothermal 9100 apparatus, and infrared spectra were recorded on a Shimadzu IR-470 spectrometer. The structural analysis relied on ^{1}H and ^{13}C NMR spectra taken in $CDCl_3$ with a BRUKER DRX-300 spectrometer. Product formation was monitored using thin-layer chromatography (TLC) on Merck silica gel 60 F254 plates. X-ray powder diffraction (XRD) measurements were performed with a Philips device using Cu-Kα radiation at a wavelength of 1.54 Å. Field-emission scanning electron microscopy (SEM) and energy-dispersive X-ray spectroscopy (EDX) were conducted with a TESCAN MIRA II digital scanning microscope. Vibrating sample magnetometry (VSM; Lakeshore 7407) evaluated magnetic properties at room temperature. Thermogravimetric analysis (TGA) was also performed using a DuPont 2000 thermal analysis apparatus, with a heating rate of 10 °C min^{-1} in an air atmosphere.

Preparation of $AlFe_2O_4$–MWCNT nanocomposite

Magnetic carbon nanotubes were created by dispersing 0.1 g of CNT–COOH in 150 mL of an aqueous solution containing $FeCl_2 \cdot 4H_2O$ and $Al(NO_3)_3 \cdot 9H_2O$ in a molar ratio of 2 : 1 while maintaining a nitrogen atmosphere at 80 °C. Ammonium hydroxide solution (≥25%) was then added dropwise to the mixture, which was continuously stirred mechanically. The pH of the mixture was adjusted to between 10 and 11, and the reaction was allowed to proceed for approximately 120 minutes. The resulting precipitate was collected using an external magnet, washed with water, and dried under vacuum at 80 °C.

Preparation of $AlFe_2O_4$–MWCNT–TEA nanocomposite

To prepare $AlFe_2O_4$–MWCNT–TEA, the obtained $AlFe_2O_4$–MWCNT was dispersed in 50 mL of ethanol for 20 minutes. Subsequently, triethanolamine (2 mmol) was introduced to the homogeneous mixture of $AlFe_2O_4$–MWCNT, which was then stirred under reflux for 24 hours. Once cooled to room temperature, the final product was extracted using a permanent magnet, washed three times with ethanol, and dried under vacuum at 60 °C.

Preparation of $AlFe_2O_4$–MWCNT–TEA–Ni(II) nanocomposite

$AlFe_2O_4$–MWCNT–TEA was suspended in 30 mL of deionized water for 30 minutes. Next, a solution of $Ni(Cl)_2 \cdot 6H_2O$ (0.073 g, 0.00025 mmol) dissolved in 5 mL of water was added to the $AlFe_2O_4$–MWCNT–TEA mixture, which was stirred at 90 °C for eight hours. Afterward, the $AlFe_2O_4$–MWCNT–TEA–Ni(II) was collected using magnetic filtration and washed three times with deionized water and ethanol; then the magnetic precipitate was dried under vacuum at 80 °C.

For the synthesis of 5-substituted 1*H*-tetrazoles using AlFe$_2$O$_4$–MWCNT–TEA–Ni(II)

As a catalyst, a mixture of an aromatic aldehyde (1 mmol), hydroxylamine (1.2 mmol), sodium azide (1.3 mmol), and the AlFe$_2$O$_4$–MWCNT–TEA–Ni(II) nanocomposite (0.005 g) was dissolved in 3 mL of DMF and magnetically stirred at 70 °C for a specified duration (as indicated in Table 2). TLC monitored the progress of the reaction (eluent: EtOAc/hexane). Once the reaction was complete, the mixture was allowed to cool to room temperature, and an external magnet was used to separate the catalyst. The solvent was evaporated under reduced pressure, and the residue was dissolved in 5 mL of water. Subsequently, 15 mL of 2 N HCl was added and stirred to facilitate the precipitation of the tetrazole in powder form. The precipitate was filtered and recrystallized from a mixture of ethanol and water, and no further purification by column chromatography was required.

NMR data of synthesized compounds
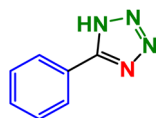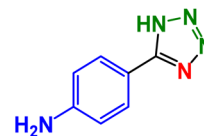
5-Phenyl-1*H*-tetrazole

^{1}HNMR (400 MHz, CDCl$_3$): 8.26 (d, *J* = 8.0 Hz, 2H), 7.53–7.47 (m, 3H), 6.34 (s, 1H) ppm; ^{13}C (100 MHz, CDCl$_3$): 155.4, 131.9, 130.7, 128.3, 127.6, 125.2 ppm.
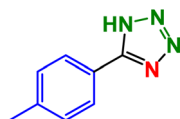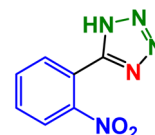
5-(*p*-Tolyl)-1*H*-tetrazole

^{1}HNMR (400 MHz, CDCl$_3$): 8.16 (d, *J* = 7.7 Hz, 2H), 7.53 (d, *J* = 8.6 Hz, 2H), 6.33 (s, 1H), 2.34 (s, 3H) ppm; ^{13}C (100 MHz, CDCl$_3$): 155.4, 130.9, 129.1, 127.2, 125.8, 21.0 ppm.
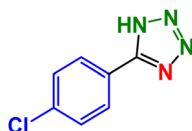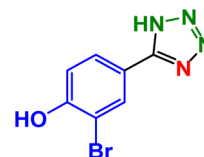
5-(4-Chlorophenyl)-1*H*-tetrazole

M.P: 259–261 °C. ^{1}HNMR (400 MHz, CDCl$_3$): 8.13 (d, *J* = 7.8 Hz, 2H), 7.55 (d, *J* = 8.0 Hz, 2H), 6.33 (s, 1H) ppm; ^{13}C (100 MHz, CDCl$_3$): 155.6, 135.2, 129.4, 128.1, 126.7 ppm.
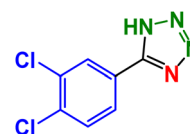
4-(1*H*-Tetrazol-5-yl)aniline

M.P: 264–266 °C. ^{1}HNMR (400 MHz, CDCl$_3$): 7.90 (d, *J* = 7.9 Hz, 2H), 6.71 (d, *J* = 7.4 Hz, 2H), 6.33 (s, 1H), 5.24 (s, 2H) ppm; ^{13}C (100 MHz, CDCl$_3$): 163.0, 150.3, 133.2, 129.0, 128.5, 127.3, 125.1 ppm.
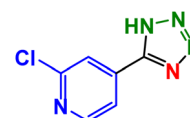
5-(2-Nitrophenyl)-1*H*-tetrazole

M.P: 155–157 °C. ^{1}HNMR (400 MHz, CDCl$_3$): 7.84 (dd, *J* = 9.3, 4.1 Hz, 2H), 7.73–7.68 (m, 1H), 7.46–7.42 (m, 1H), 6.33 (s, 1H) ppm; ^{13}C (100 MHz, CDCl$_3$): 155.6, 131.2, 129.0, 126.5, 126.1, 124.3 ppm.

2-Bromo-4-(1*H*-tetrazol-5-yl)phenol

M.P: 173–175 °C. ^{1}HNMR (400 MHz, CDCl$_3$): 9.01 (s, 1H), 7.76 (d, *J* = 8.6 Hz, 1H), 7.34 (s, 1H), 6.89 (d, *J* = 8.0 Hz, 1H), 6.33 (s, 1H) ppm; ^{13}C (100 MHz, CDCl$_3$): 157.8, 155.4, 133.6, 129.4, 125.1, 119.0, 114.2 ppm.
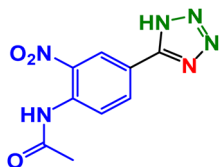
5-(3,4-Dichlorophenyl)-1*H*-tetrazole

M.P: 148–150 °C. ^{1}HNMR (400 MHz, CDCl$_3$): 9.01 (s, 1H), 7.76 (d, *J* = 8.6 Hz, 1H), 7.34 (s, 1H), 6.89 (d, *J* = 8.0 Hz, 1H), 6.33 (s, 1H) ppm; ^{13}C (100 MHz, CDCl$_3$): 157.8, 155.4, 133.6, 129.4, 125.1, 119.0, 114.2 ppm.
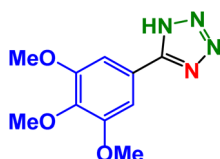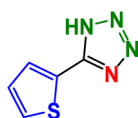
2-Chloro-4-(1*H*-tetrazol-5-yl)pyridine

M.P: 198–200 °C. ^{1}HNMR (400 MHz, CDCl$_3$): 8.72 (d, J = 8.0 Hz, 1H), 8.37 (d, J = 8.4 Hz, 1H), 7.95 (s, 1H), 6.33 (s, 1H) ppm; ^{13}C (100 MHz, CDCl$_3$): 155.6, 148.9, 144.9, 140.1, 114.3, 112.5.

## *N*-(2-Nitro-4-(1*H*-tetrazol-5-yl)phenyl)acetamide

M.P: 210–212 °C. ^{1}HNMR (400 MHz, CDCl$_3$): 9.81 (s, 1H), 8.79 (s, 1H), 8.58 (d, J = 8.0 Hz, 1H), 8.11 (d, J = 7.6 Hz, 1H), 6.33 (s, 1H), 2.08 (s. 3H) ppm; ^{13}C (100 MHz, CDCl$_3$): 168.9, 155.7, 143.2, 133.7, 131.0, 127.6, 123.1, 24.3 ppm.

5-(3′,4′,5′-Trimethoxyphenyl)tetrazole

M.P: 200–202 °C. ^{1}HNMR (400 MHz, CDCl$_3$): 7.01 (s, 2H), 6.33 (s, 1H), 3.90 (s, 6H), 3.76 (s. 3H) ppm; ^{13}C (100 MHz, CDCl$_3$): 158.5, 155.1, 140.9, 124.6, 104.3, 63.9, 55.4 ppm.

5-(Thiophen-2-yl)-1*H*-tetrazole

M.P: 201–203 °C. ^{1}HNMR (400 MHz, CDCl$_3$): 7.82 (d, J = 7.8 Hz, 1H), 7.65 (d, J = 8.6 Hz, 1H), 7.06–7.02 (m, 1H), 6.33 (s, 1H) ppm; ^{13}C (100 MHz, CDCl$_3$): 163.2, 143.5, 129.6, 128.6, 128.1 ppm.
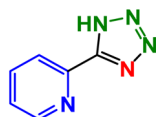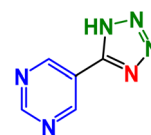
2-(1*H*-Tetrazol-5-yl)pyridine

M.P: 210–212 °C. ^{1}HNMR (400 MHz, CDCl$_3$): 8.63 (d, J = 8.0 Hz, 1H), 8.35 (d, J = 8.0 Hz, 1H), 7.47–7.43 (m, 1H), 7.28–7.23 (m, 1H), 6.33 (s, 1H) ppm; ^{13}C (100 MHz, CDCl$_3$): 163.2, 154.0, 148.7, 137.6, 125.6, 123.1 ppm.
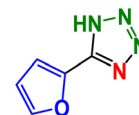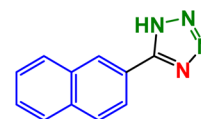
5-(Furan-2-yl)-1*H*-tetrazole

M.P: 201–203 °C. ^{1}HNMR (400 MHz, CDCl$_3$): 8.22 (d, J = 7.6 Hz, 1H), 7.45 (d, J = 8.0 Hz, 1H), 6.73–6.70 (m, 1H), 6.33 (s, 1H) ppm; ^{13}C (100 MHz, CDCl$_3$): 163.7, 155.1, 142.8, 111.4, 108.3 ppm.

5-(1*H*-Pyrrol-2-yl)-1*H*-tetrazole

M.P: 224–226 °C. ^{1}HNMR (400 MHz, CDCl$_3$): 9.26 (s, 1H), 7.04 (d, J = 7.7 Hz, 1H), 6.68 (d, J = 7.6 Hz, 1H), 6.33 (s, 1H), 6.23–6.20 (m, 1H) ppm; ^{13}C (100 MHz, CDCl$_3$): 163.2, 128.3, 120.7, 112.6, 106.7 ppm.

5-(1*H*-Tetrazol-5-yl)pyrimidine

M.P: 253–255 °C. ^{1}HNMR (400 MHz, CDCl$_3$): 9.34 (s, 1H), 9.04 (s, 2H), 6.43 (s, 1H) ppm; ^{13}C (100 MHz, CDCl$_3$): 164.0, 150.7, 147.4, 131.1 ppm.

5-(Naphthalen-2-yl)-1*H*-tetrazole

M.P: 202–204 °C. ^{1}HNMR (400 MHz, CDCl$_3$): 9.06 (s, 1H), 8.17 (d, J = 8.0 Hz, 1H), 8.04 (d, J = 7.7 Hz, 1H), 7.64 (d, J = 7.4 Hz, 1H), 7.47 (d, J = 8.6 Hz, 1H), 7.36–7.29 (m, 2H), 6.33 (s, 1H) ppm; ^{13}C (100 MHz, CDCl$_3$): 157.4, 135.1, 133.2, 129.9, 128.3, 127.6, 125.3 ppm.
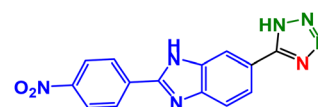
2-(4-Nitrophenyl)-6-(1*H*-tetrazol-5-yl)-1*H*-benzo[*d*]imidazole

M.P: 276–278 °C. ^{1}HNMR (400 MHz, CDCl$_3$): 9.34 (s, 1H), 9.04 (s, 2H), 6.43 (s, 1H) ppm; ^{13}C (100 MHz, CDCl$_3$): 164.0, 150.7, 147.4, 131.1 ppm.
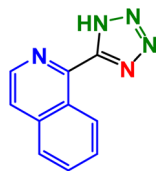
1-(1H-Tetrazol-5-yl)isoquinoline

M.P: 235–237 °C. ^{1}HNMR (400 MHz, CDCl$_3$): 8.73 (d, J = 7.8 Hz, 1H), 8.09 (d, J = 8.0 Hz, 1H), 7.71 (d, J = 8.6 Hz, 1H), 7.46–7.41 (m, 3H), 6.33 (s, 1H) ppm; ^{13}C (100 MHz, CDCl$_3$): 163.0, 160.5, 143.1, 138.7, 133.2, 130.8, 129.7, 128.1, 127.0, 126.4, 118.6 ppm.

Conclusion

This study set out to pioneer the development and assessment of a groundbreaking magnetic nanocatalyst, AlFe$_2$O$_4$–MWCNT–TEA–Ni(II), for the multicomponent synthesis of 5-substituted-1H-tetrazoles. The catalyst, a unique amalgamation of AlFe$_2$O$_4$ magnetic nanoparticles, multiwalled carbon nanotubes (MWCNTs), stabilized with triethanolamine (TEA), and coordinated with nickel(II) ions, was put to the test by conducting the reaction at 50 °C in dimethylformamide (DMF) using aromatic aldehydes, hydroxylamine, and sodium azide as reactants. The optimization of parameters such as temperature, catalyst amount, and reaction time led to the achievement of high yields, marking a significant advancement in the field.

The catalyst efficiently facilitated the formation of high-yield tetrazole derivatives, with the magnetic core enabling easy separation and reuse, demonstrating its practicality and sustainability. The inclusion of MWCNTs enhanced surface area and catalytic efficiency, while Ni(II) promoted effective reaction kinetics. This approach aligns with green chemistry principles, offering an economical and environmentally friendly method for synthesizing valuable heterocycles relevant to pharmaceuticals and agrochemicals. Future research may explore a broader range of substrates and reaction conditions to optimize performance further and extend industrial applications. Overall, this study highlights the potential of integrating magnetic materials with catalytic systems to develop advanced, sustainable methods for organic synthesis, addressing current limitations and fostering innovation in the field.

Data availability

No primary research results, software or code have been included and no new data were generated or analyzed as part of this review.

Conflicts of interest

The authors declare no conflict of interest.

References

1 J. Jin, R. Xu, X. Wu, X. Fang, W. Kong, K. Zhang and J. Cheng, *Tetrahedron*, 2023, **132**, 133261.

2 D. P. Zarezin, A. M. Kabylda, V. I. Vinogradova, P. V. Dorovatovskii, V. N. Khrustalev and V. G. Nenajdenko, *Tetrahedron*, 2018, **74**, 4315–4332.

3 R. Javahershenas, H. Mei, M. Koleyc, V. A. Soloshonokd and A. Makarem, *Synthesis*, 2024, **56**, 2445–2461.

4 S. Jaiswal, K. Verma, J. Dwivedi and S. Sharma, *Eur. J. Med. Chem.*, 2024, **271**, 116388.

5 C. G. Neochoritis, T. Zhao and A. Dömling, *Chem. Rev.*, 2019, **119**, 1970–2042.

6 C. X. Wei, M. Bian and G. H. Gong, *Molecules*, 2015, **20**, 5528–5553.

7 L. V. Myznikov, A. Hrabalek and G. I. Koldobskii, *Chem. Heterocycl. Compd.*, 2007, **43**, 1–9.

8 R. J. Herr, *Bioorg. Med. Chem.*, 2002, **10**, 3379–3393.

9 S. Y. Kang, S. H. Lee, H. J. Seo, M. E. Jung, K. Ahn, J. Kim and J. Lee, *Bioorg. Med. Chem. Lett.*, 2008, **18**, 2385–2389.

10 P. D. Boatman, T. O. Schrader, M. Kasem, B. R. Johnson, P. J. Skinner, J. K. Jung, J. Xu, M. C. Cherrier, P. J. Webb and G. Semple, *Bioorg. Med. Chem. Lett.*, 2010, **20**, 2797–2800.

11 B. C. H. May and A. D. Abell, *J. Chem. Soc., Perkin Trans. 1*, 2002, **172**, 172–178.

12 C. Liljebris, S. D. Larsen, D. Ogg, B. J. Palazuk and J. E. Bleasdale, *J. Med. Chem.*, 2002, **45**, 1785–1798.

13 G. Ortar, A. Schiano Moriello, M. G. Cascio, L. De Petrocellis, A. Ligresti, E. Morera, M. Nalli and V. Di Marzo, *Bioorg. Med. Chem. Lett.*, 2008, **18**, 2820–2824.

14 V. V. Zarubaev, E. L. Golod, P. M. Anfimov, A. A. Shtro, V. V. Saraev, A. S. Gavrilov, A. V. Logvinov and O. I. Kiselev, *Bioorg. Med. Chem.*, 2010, **18**, 839–848.

15 J. H. Toney, P. M. D. Fitzgerald, N. Grover-Sharma, S. H. Olson, W. J. May, J. G. Sundelof, D. E. Vanderwall, K. A. Cleary, S. K. Grant and J. K. Wu, *Chem. Biol.*, 1998, **5**, 185–196.

16 C. C. Eze, A. M. Ezeokonkwo, I. D. Ugwu, U. F. Eze, E. L. Onyeyilim, I. S. Attah and I. V. Okonkwo, *Anti Cancer Agents Med. Chem.*, 2022, **22**, 2822–2851.

17 S. A. F. Rostom, H. M. A. Ashour, H. A. A. Razik, H. Abd El Fattah and N. N. El-Din, *Bioorg. Med. Chem.*, 2009, **17**, 2410–2422.

18 M. K. M. Ramalingam and S. Rajagopalan, *J. Med. Chem. Sci.*, 2023, **6**, 2432–2448.

19 L. Zhang, *et al.*, *J. Med. Chem.*, 2016, **59**, 1233–1247.

20 S. Manzoor, Q. Tariq, X. Yin and J. G. Zhang, *Def. Technol.*, 2021, **17**, 1995–2010.

21 A. A. Dippold, D. Izsák, T. M. Klapötke and C. Pflüger, *Chem. – Eur. J.*, 2016, **22**, 1768–1778.

22 A. N. Reznikov, V. A. Ostrovskii and Y. N. Klimochkin, Synthesis of Nonracemic Tetrazole GABA Analogs, *Russ. J. Org. Chem.*, 2018, **54**, 1715–1721.

23 K. Karaghiosoff, T. M. Klapötke, P. Mayer, H. Piotrowski, K. Polborn, R. L. Willer, J. J. Weigand and R. V. July, *J. Org. Chem.*, 2006, **71**, 1295.

24 D. Kumar, C. He, L. A. Mitchell, D. A. Parrish and J. M. Shreeve, *J. Mater. Chem. A*, 2016, **4**, 9220.

25 Y. Tang, C. He, G. H. Imler, D. A. Parrish and J. M. Shreeve, *J. Mater. Chem. A*, 2016, **4**, 13923.

26 D. Kumar, G. H. Imler, D. A. Parrish and J. M. Shreeve, *J. Mater. Chem. A*, 2017, **5**, 16767.

27 J. Zhu, Q. Wang and M. X. Wang, *Multi-Component Reactions in Organic Synthesis*, Wiley-VCH, Weinheim, 2015.

28 T. J. J. Müller, R. Javahershenas and S. Nikzat, *RSC Adv.*, 2023, **13**, 16619.

29 R. Javahershenas, *J. Mol. Liq.*, 2023, **385**, 122398.

30 S. Imeni, A. Makarem and R. Javahershenas, *Asian J. Org. Chem.*, 2023, e202300303.

31 R. Javahershenas, A. Makarem and K. D. Klika, *RSC Adv.*, 2024, **14**, 5547–5565.

32 R. Javahershenas, J. Han, M. Kazemi and P. J. Jervise, *ChemistrySelect*, 2024, **9**, e202401496.

33 R. Javahershenas, J. Han, M. Kazemi and P. J. Jervise, *ChemistryOpen*, 2024, **13**, e202400185.

34 M. Jawaid, A. Khan, *Carbon Composite Catalysts: Preparation, Structural and Morphological Property and Applications*, Springer, 2022, DOI: 10.1007/978-981-19-1750-9.

35 R. Javahershenas, V. A. Soloshonok, K. D. Klika and P. J. Jervis, *Carbon Lett.*, 2025, **35**, 385.

36 M. S. Dresselhaus, G. Dresselhaus and P. Avouris, *Carbon Nanotubes: Synthesis, Structure, Properties, and Applications*, Springer Berlin Heidelberg, 2001, DOI: 10.1007/3-540-39947-X.

37 A. K. Jagadeesan, K. Thangavelu and V. Dhananjeyan, *Carbon Nanotubes: Synthesis, Properties and Applications In 21st Century Surface Science – A Handbook*, IntechOpen, 2020, DOI: 10.5772/intechopen.92995.

38 R. Dubey, D. A. S. Dutta and P. Chattopadhyay, *Nanoscale Adv.*, 2021, **3**, 5722–5744.

39 N. Anzar, R. Hasan, M. Tyagi, N. Yadav and J. Narang, *Sens. Int.*, 2020, **1**, 100003.

40 N. Gupta, S. M. Gupta and S. K. Sharma, *Carbon Lett.*, 2019, **29**, 419–447.

41 Y. Yan, J. Miao, Z. Yang, F. X. Xiao, H. B. Yang, B. Liu and Y. Yang, *Chem. Soc. Rev.*, 2015, **44**, 3295–3346.

42 A. Bahuguna, A. Kumar and V. Krishnan, *Asian J. Org. Chem.*, 2019, **8**, 1263–1305.

43 C. Testa, A. Zammataro, A. Pappalardo and G. T. Sfrazzetto, *RSC Adv.*, 2019, **9**, 27659–27664.

44 E. Pérez-Mayoral, M. Godino-Ojer, L. M. Pastrana-Martínez, S. Morales-Torres and F. J. Maldonado-Hódar, *ChemCatChem*, 2023, e202300961.

45 T. Mori, H. Tanaka, A. Dalui, N. Mitoma, K. Suzuki, M. Matsumoto, N. Aggarwal, A. Patnaik, A. Acharya and L. K. Shrestha, *Angew. Chem., Int. Ed.*, 2018, **130**, 9827–9831.

46 M. M. Titirici, R. J. White, N. Brun, V. L. Budarin, D. S. Su, F. del Monte, J. H. Clark and M. J. MacLachlan, *Chem. Soc. Rev.*, 2015, **44**, 250–290.

47 V. Polshettiwar and R. S. Varma, *Green Chem.*, 2010, **12**, 743–754.

48 M. Kumar and Y. Ando, *J. Nanosci. Nanotechnol.*, 2010, **10**, 3739–3758.

49 A. Eatemadi, H. Daraee, H. Karimkhanloo, M. Kouhi, N. Zarghami, A. Akbarzadeh, M. Abasi, Y. Hanifehpour and S. W. Joo, *Nanoscale Res. Lett.*, 2014, **9**, 393.

50 M. Nasrollahzadeh, Z. Nezafat, N. S. S. Bidgoli and N. Shafiei, *Mol. Catal.*, 2021, **513**, 111788.

51 M. Nasrollahzadeh, M. Sajjadi, H. Ghafuri, N. S. S. Bidgoli, A. J. L. Pombeiro and S. Hazra, *Coord. Chem. Rev.*, 2021, **446**, 214132.

52 R. Javahershenas, H. Mei, M. Koley, V. A. Soloshonok and A. Makarem, *Synthesis*, 2024, **56**, 2445–2461.

53 S. V. Voitekhovich, O. A. Ivashkevich and P. N. Gaponik, *Russ. J. Org. Chem.*, 2013, **49**, 635–654.

54 G. Aromí, L. A. Barrios, O. Roubeau and P. Gamez, *Coord. Chem. Rev.*, 2011, **255**, 485–546.

55 H. S. Lihumis, Z. A. Al Talebi and S. H. Shanan, *Asian J. Green Chem.*, 2022, **6**, 68.

56 S. Swami, S. N. Sahu and R. Shrivastava, *RSC Adv.*, 2021, **11**, 39058–39086.

57 S. Leyva-Ramos and J. Cardoso-Ortiz, *Curr. Org. Chem.*, 2021, **25**, 388–403.

58 A. Sarvary and A. Maleki, *Mol. Diversity*, 2015, **19**, 189–212.

59 L. V. Chanu and O. M. Singh, *J. Heterocycl. Chem.*, 2021, **58**, 2207–2225.

60 R. Mittal, A. Kumar and S. K. Awasthi, *RSC Adv.*, 2021, **11**, 11166–11176.

61 M. Gao, L. Wang, Y. Yang, Y. Sun, X. Zhao and Y. Wan, *ACS Catal.*, 2023, 4060–4090.

62 D. Wei, X. Shi, R. Qu, K. Junge, H. Junge and M. Beller, *ACS Energy Lett.*, 2022, **7**, 3734–3752.

63 S. Jaiswal, J. Dwivedi, D. Kishore and S. Sharma, *Curr. Org. Chem.*, 2024, **28**, 134–160.

64 A. Ghorbani-Choghamarani, M. Mohammadi, L. Shiri and Z. Taherinia, *Res. Chem. Intermed.*, 2019, **45**, 5705–5723.

65 M. Cherfi, T. Harit, M. Amanchar, A. Oulous and F. Malek, *Organics*, 2024, **5**, 575–597.

66 M. Mahyari and A. Shaabani, *J. Mater. Chem. A*, 2014, **2**, 16652–16659.

67 S. D. Guggilapu, S. K. Prajapti, A. Nagarsenkar, K. K. Gupta and B. N. Babu, *Synlett*, 2016, **27**, 1241–1244.

68 M. Abdollahi-Alibeik and A. Moaddeli, *New J. Chem.*, 2015, **39**, 2116–2122.

69 B. Mitra, S. Mukherjee, G. C. Pariyar and P. Ghosh, *Tetrahedron Lett.*, 2018, **14**, 1385–1389.

70 M. Sridhar, K. K. R. Mallu, R. Jillella, K. R. Godala, C. R. Beeram and N. Chinthala, *Synthesis*, 2013, **45**, 507–510.

71 U. B. Patil, K. R. Kumthekar and J. M. Nagarkar, *Tetrahedron Lett.*, 2012, **53**, 3706–3709.

72 M. M. Heravi, A. Fazeli, H. A. Oskooie, Y. S. Beheshtiha and H. Valizadeh, *Synlett*, 2012, **23**, 2927–2930.

73 S. Behrouz, *J. Saudi Chem. Soc.*, 2017, **21**, 220–228.

74 K. M. Khan, I. Fatima, S. M. Saad, M. Taha and W. Voelter, *Tetrahedron Lett.*, 2016, **57**, 523–524.

75 P. Akbarzadeh, N. Koukabi, E. Kolvari, *Mol. Diversity*, 2019, DOI: 10.1007/s11030-019-09951-6.